University of Bath

Alternative formats
If you require this document in an alternative format, please contact:
openaccess@bath.ac.uk

Robotic reverberation mapping of the broad-line radio galaxy 3C 120

Michael Hlabathe[1,2]⋆, David Starkey[3], Keith Horne[3], Encarni Romero-Colmenero[2,4], Steven Crawford[5], Stefano Valenti[6,7], Hartmut Winkler[8], Aaron Barth[9], Christopher Onken[10], David Sand[11], Tommaso Treu[12], Aleksandar Diamond-Stanic[13], Carolin Villforth[14]

[1] *University of Cape Town, Private Bag X3, Rondebosch 7701, South Africa*
[2] *South African Astronomical Observatory, P.O Box 9, Observatory 7935, Cape Town, South Africa*
[3] *SUPA Physics and Astronomy, University of St. Andrews, Fife, KY16 9SS, Scotland, UK*
[4] *Southern African Large Telescope Foundation, P.O Box 9, Observatory 7935, Cape Town, South Africa*
[5] *Space Telescope Science Institute, 3700 San Martin Drive, Baltimore, MD 21218, USA*
[6] *Department of Physics, University of California, 1 Shields Avenue, Davis, CA 95616-5270, USA*
[7] *Las Cumbres Observatory Global Telescope Network, 6740 Cortona Drive, Suite 102, Goleta, CA 93117, USA*
[8] *Department of Physics, University of Johannesburg, P.O. Box 524, 2006 Auckland Park, South Africa*
[9] *Department of Physics and Astronomy, University of California, 4129 Frederick Reines Hall, Irvine, CA, 92697-4575, USA*
[10] *Research School of Astronomy and Astrophysics, Australian National University, Canberra ACT 2611, Australia*
[11] *Department of Astronomy/Steward Observatory, 933 North Cherry Avenue, Room N204, Tucson, AZ 85721-0065, USA*
[12] *Department of Physics and Astronomy, University of California, Los Angeles, CA 90095-1547, USA*
[13] *Department of Physics and Astronomy, Bates College, 44 Campus Avenue, Lewiston ME 04240, USA*
[14] *Department of Physics, University of Bath, Claverton Down Road, Bath BA2 7AY, UK*

ABSTRACT

We carried out photometric and spectroscopic observations of the well-studied broad-line radio galaxy 3C 120 with the Las Cumbres Observatory (LCO) global robotic telescope network from 2016 December to 2018 April as part of the LCO AGN Key Project on Reverberation Mapping of Accretion Flows. Here, we present both spectroscopic and photometric reverberation mapping results. We used the interpolated cross-correlation function (ICCF) to perform multiple-line lag measurements in 3C 120. We find the Hγ, He II λ4686, Hβ and He I λ5876 lags of $\tau_{\mathrm{cen}} = 18.8^{+1.3}_{-1.0}$, $2.7^{+0.7}_{-0.8}$, $21.2^{+1.6}_{-1.0}$, and $16.9^{+0.9}_{-1.1}$ days respectively, relative to the V-band continuum. Using the measured lag and rms velocity width of the Hβ emission line, we determine the mass of the black hole for 3C 120 to be $M = \left(6.3^{+0.5}_{-0.3}\right) \times 10^7 \,(f/5.5)\,\mathrm{M}_\odot$. Our black hole mass measurement is consistent with similar previous studies on 3C 120, but with small uncertainties. In addition, velocity-resolved lags in 3C 120 show a symmetric pattern across the Hβ line, 25 days at line centre decreasing to 17 days in the line wings at ± 4000 km s^{-1}. We also investigate the inter-band continuum lags in 3C 120 and find that they are generally consistent with $\tau \propto \lambda^{4/3}$ as predicted from a geometrically-thin, optically-thick accretion disc. From the continuum lags, we measure the best fit value $\tau_0 = 3.5 \pm 0.2$ days at $\lambda_0 = 5477$Å. It implies a disc size a factor of 1.6 times larger than prediction from the standard disc model with $L/L_{\mathrm{Edd}} = 0.4$. This is consistent with previous studies in which larger than expected disc sizes were measured.

Key words: Seyfert-galaxies; quasars-galaxies; nuclei-galaxies; individual (3C 120) - galaxies; emission-lines; super-massive black holes; accretion discs; accretion

1 INTRODUCTION

It is believed that every active galactic nucleus (AGN) is powered by a supermassive black hole (BH) at its centre

⋆ E-mail: mh@saao.ac.za

(Lynden-Bell & Rees 1971). For a detailed description of AGN and their different components, otherwise known as the unified model of an AGN, see Antonucci (1993); Urry & Padovani (1995). The supermassive BH in active galactic nuclei are believed to play a pivotal role in galaxy formation, thus encouraging efforts to understand their growth and distribution of mass over cosmological time.

In particular, the observed scaling relationships between BH mass M and host-galaxy properties, such as the velocity dispersion of the bulge stars $M - \sigma_*$ (Ferrarese & Merritt 2000; Gebhardt et al. 2000) or the bulge luminosity $M - L_{\mathrm{bulge}}$ (Kormendy & Richstone 1995; Magorrian et al. 1998), indicate a strong connection between galaxy evolution and BH growth. To further investigate the nature of the BH-galaxy co-evolution, more BH masses must be accurately determined in both nearby galaxies and more distant AGNs. Dynamical methods based on high angular resolution kinematics of stars and gas have been widely used to measure masses of BHs in nearby galaxies (Kormendy & Gebhardt 2001; Ferrarese & Ford 2005). However, they are limited to the spatially resolved kinematics of nearby (few tens of Mpc) galaxies even with the current technology. Yet, in Type 1 AGNs, the broad emission lines from the broad-line region (BLR) can be used to probe the inner structure of the AGN and therefore determine M via a technique known as reverberation mapping (Blandford & McKee 1982; Peterson 1993, 2001).

Reverberation mapping (RM) measures the mean time delay or lag τ between changes in the continuum from the accretion disc and corresponding changes in the broad emission lines, thus allowing for the direct measurement of the BLR size ($R_{BLR} = c\tau$) assuming light-travel time effects. Typically, the time delay is found using traditional cross-correlation methods, such as the interpolation cross-correlation function (ICCF, Gaskell & Sparke 1986; Gaskell & Peterson 1987; White & Peterson 1994) or the discrete correlation function (DCF, Edelson & Krolik 1988). Over time, other approaches have been introduced for lag determination, such as Stochastic Process Estimation for AGN Reverberation (SPEAR and/or python implementation JAVELIN, Zu et al. 2011) and quite recently the Continuum REprocessed AGN Markov Chain (CREAM, Starkey et al. 2016, 2017), which have been found to perform better statistically on data with seasonal gaps or irregular sampling than the traditional methods (Grier et al. 2017b; Li et al. 2017).

By combining the measured τ and the velocity width ΔV (either from FWHM or line dispersion σ_{line}) of the broad emission line, and assuming virialized motions of the gas within the BLR, we can estimate the central black hole mass as

$$M = f \frac{c \, \tau \, \Delta V^2}{G}, \tag{1}$$

where τ is the measured lag of the broad emission line, c is the speed of light, G is the gravitational constant, and f is a dimensionless factor which takes the structure, kinematics and orientation effects of the BLR into account.

RM has been applied successfully in multiple spectroscopic campaigns, yielding > 50 BH masses to date (e.g. Wandel et al. 1999; Kaspi et al. 2000; Peterson et al. 2004; Bentz et al. 2009b; Denney et al. 2009a; Barth et al. 2011,

2015; Valenti et al. 2015; Shen et al. 2016; Fausnaugh et al. 2017; Grier et al. 2018; Du et al. 2018a), see also Bentz & Katz (2015). Although RM can be used to find BH masses in nearby and distant AGNs, it does, however, require long-term monitoring, high cadence and signal-to-noise, which is observationally hard to achieve using ground-based telescopes. Fortunately, RM also provides a scaling relationship between BLR size and the AGN luminosity at 5100Å ($R_{BLR} - L_{5100}$) (e.g., Bentz et al. 2013), thus allowing for the measurement of BH mass using single-epoch spectrum of the AGN (e.g., Wandel et al. 1999; Vestergaard 2002).

RM can also be used to provide some insight into the structure and size of the accretion disc in AGN using the wavelength-dependent continuum delays, wherein ionizing photons from a compact region near BH propagate outwards and is reprocessed into UV/Optical continuum emission with light-travel time delays that increase with wavelength (e.g. Cackett et al. 2007). By measuring the continuum time delay τ as a function of wavelength λ, RM can probe the radial temperature profile of the accretion disc and test the $\tau \propto \lambda^{4/3}$ prediction of the standard thin-disc model of Shakura & Sunyaev (1973).

Here, we undertake a robotic RM study of 3C 120 (Table 1) from long-term monitoring with the Las Cumbres Observatory (LCO) global robotic telescope network. 3C 120 was shown to exhibit a type 1 Seyfert spectrum by Sargent (1967) and it was one of the first radio sources for which variability was confirmed (Pauliny-Toth & Kellermann 1966). Furthermore, 3C 120 became the subject of much interest when the apparent superluminal motion of its radio jet was discovered (Walker 1997; Gómez et al. 2011).

3C 120 has also been the subject of several previous reverberation studies over the years. Observational campaigns in the late 1990's (Peterson et al. 1998b), later reanalysed by Peterson et al. (2004) determined a time lag of ~ 40 days between the continuum and the Hβ line. Kollatschny et al. (2014) performed a reverberation analysis of a set of 3C 120 optical spectra secured between 2008 September and 2009 March, concluding that the Hβ lag relative to the continuum is $27.9^{+7.1}_{-5.9}$ days. Du et al. (2018b) determined the Hβ-to-continuum delay to be $20.2^{+5.0}_{-4.2}$ days. 3C 120 has also been the subject of infrared dust reverberation mapping by Ramolla et al. (2018). Using our high signal-to-noise observations, we aim to accurately determine M in 3C 120 along with measuring the inter-band continuum lags.

We arranged this paper as follows: in Section 2 we describe the observations and data reduction. Section 3 reviews the time-series analysis methodology. Section 4 presents the inter-band continuum delays in context with the standard accretion disc theory. Section 5 presents the black hole mass measurements. In Section 6, we investigate the structure and kinematics of the BLR in 3C 120. We discuss our results and summarize our conclusions in Sections 7 and 8 respectively. We assumed a cosmological model with $H_0 = 73.0$ km s^{-1} Mpc^{-1}, $\Omega_m = 0.27$ and $\Omega_\Lambda = 0.73$.

2 OBSERVATIONS AND DATA REDUCTION

To carry out a reverberation mapping analysis on 3C 120, we require continuum light curve(s) which we measure

Table 1. Object properties

Object	RA[(1)] (J2000)	DEC[(1)] (J2000)	$D_L^{(2)}$ (Mpc)	$z^{(1)}$
3C 120	04 33 11.1	+05 21 16	139	0.0330

[1] Values from NED database.
[2] Adopted luminosity distance for our cosmological model.

from photometry and emission-line light curve(s) from spectroscopy. The data employed here were acquired as part of the Las Cumbres Observatory (LCO) AGN Key Project titled Reverberation Mapping of AGN Accretion Flows (Valenti et al. 2015). The observations include 6-band photometric imaging (Section 2.1) and FLOYDS spectroscopy (Section 2.2).

2.1 Photometry

Our photometric monitoring campaign of 3C 120 in 6 bands (U, g', V, r', i', z_s) ran from 2016 December to 2018 April using the LCO 1m robotic telescopes (Brown et al. 2013) deployed at Siding Spring Observatory (SSO), South African Astronomical Observatory (SAAO), McDonald Observatory (McD) and Cerro Tololo Interamerican Observatory (CTIO). A journal of photometric observations is presented in Table 2, and the resulting light curves in Figure 2. All observations were taken with Sinistro, a 4k×4k-pixel quad-readout CCD camera with a 26.5×26.5 arcmin field of view and a pixel scale of 0.389 arcsec/pixel. We obtained 563 observations in the Johnson V filter, 432 in the Johnson U filter, 508 in the SDSS g' filter, 498 in the SDSS r' filter, 480 in the SDSS i' filter and 460 in the Pan-STARRS z_s filter with nearly daily cadence during 50 nights before and 250 nights after the 100-day solar conjunction gap.

The basic data reduction steps were carried out using the LCO BANZAI data pipeline (Brown et al. 2013), which performs flat fielding and bias subtraction. Subsequent to this, all images were cleaned of cosmic rays applying the L.A.Cosmic algorithm (van Dokkum 2001).

To construct differential light curves in the respective bands, we performed a multi-aperture photometry in AstroImageJ. AstroImageJ is an image analysis tool designed to automatically go through a set of time-series images and measure light curves (Collins et al. 2017).

We analyzed the dataset from each filter separately but in the same manner. Firstly, we aligned the V images using *Align stack using WCS* functionality in AstroImageJ. Using visual inspection, we selected from a set of aligned images, one of the images with the best seeing. We selected 5 comparison stars on the basis of their brightness and relative isolation (Figure 1). We then measured the FWHM in pixels of those stars using *Plot seeing profile* in AstroImageJ, and recorded the measurements. Next, we randomly selected 20 more images from the set and measured the FWHM of the comparison stars. We then combined all the measured FWHM to produce the average. Using the average value, an aperture radius and sky annulus radii were then determined as recommended in Collins et al. (2017). This resulted in an aperture radius of 12 pixels (5.0 arcsec) and an inner and outer sky aperture radii of 22 and 33 pixels respectively. We
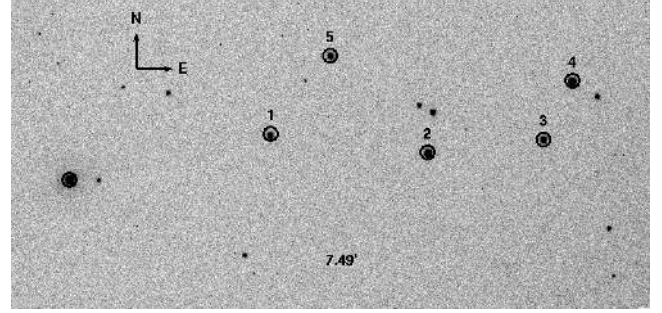
Figure 1. A cut-out of the full Sinistro V-band image of 3C 120 taken with CTIO 1m telescope. The comparison stars used in the differential photometry are indicated. Image is 7.49 arcmin across, the N and E pointers/arrows are 0.3 arcmin in length.

adopted the same aperture and sky annuli radii for all filters.

AstroImageJ produces a measurements table which includes among other parameters, sky-subtracted counts of the target and that of the chosen comparison stars. To perform differential photometry, we measure instrumental magnitudes of the target and comparison stars from the measured counts. We then selected a reference frame (first image in the set) as the zero point. We calculated the magnitude difference (Δm) of each comparison star between the reference epoch and each epoch. We also calculated the rms variability of each comparison star based on the resulting (Δm). The comparison star with lowest rms variability was selected as the main comparison star and others as check stars. For each filter, a different comparison star was selected as indicated in Table 3. We subtracted the main comparison star from the check stars ($\Delta m - \Delta m_{\rm comp}$). As a consistency check, we found the check stars to yield rms intrinsic variations of about 1%. We then also subtracted the main comparison star from the target to get the differential magnitudes of the target ($m_{\rm target} - m_{\rm comp}$). We calibrated the differential magnitudes of the target using the catalog (APASS, Henden et al. 2015) and (Pan-STARRS, Chambers et al. 2016) magnitudes of the comparison stars. As a reference U-band magnitude could not be found for the comparison stars, we estimate the U-band flux for the comparison stars based on the B-V, U-B colors (Fitzgerald 1970; Ducati et al. 2001) and assuming a 0.2 mag uncertainty on the resulting U magnitude. We then performed a conversion to AB system for Johnson U and V magnitudes (Blanton & Roweis 2007). Finally, we flux-calibrated the differential light curve of the target to mJy. The same procedure was repeated for each filter. In Table 3, we give the adopted mean AB magnitude and its uncertainty for each comparison star.

In the resulting light curves, we removed extreme outliers (verified by inspection of the images to be caused by, for example, cosmic ray hits, bad ccd pixels, strong sky gradients, clouds, etc). This left us with 541(96%) data points on the final light curve in V, 380(88%) in U, 476(94%) in g', 446(90%) in r', 439(92%) in i' and 425(92%) in z_s. We present the resulting 3C 120 light curves in each band in Figure 2. The light curves exhibit strong variations with similar structure across all the photometric bands. Several 10-20% features on 30-100 day timescales are detected with

Table 2. Summary of photometric observations for 3C 120.

Filter[1]	$\lambda_{\mathrm{pivot}}^{(2)}$	LCO site[3]	Date range[4]	t_{exp} (s)	Epochs[5]	Total[6]
U	3656Å	SAAO	20170826-20180327	300	107	432
		McD	20170810-20180315		14	
		SSO	20170806-20180207		90	
		CTIO	20170804-20180406		221	
g'	4770Å	SAAO	20170306-20180327	120	149	508
		McD	20170330-20180315		14	
		SSO	20170306-20180207		91	
		CTIO	20170309-20180406		254	
V	5477Å	SAAO	20170106-20180327	300	156	563
		McD	20170330-20180315		14	
		SSO	20161228-20180207		113	
		CTIO	20170106-20180406		280	
r'	6231Å	SAAO	20170308-20180406	120	171	498
		McD	20170405-20180306		12	
		SSO	20170306-20180404		125	
		CTIO	20170314-20180409		190	
i'	7625Å	SAAO	20170308-20180406	120	158	480
		McD	20170405-20180306		12	
		SSO	20170306-20180404		124	
		CTIO	20170314-20180309		186	
z_s	8660Å	SAAO	20170308-20180406	240	160	460
		McD	20170405-20180306		11	
		SSO	20170306-20180304		106	
		CTIO	20170314-20180409		183	

[1] The filter through which the data were taken.
[2] Filter centroid wavelength.
[3] SAAO (South African Astronomical Observatory), McD (McDonald Observatory), SSO (Siding Spring Observatory), CTIO (Cerro Tololo Interamerican Observatory).
[4] Start and end date of observations, we note the ∼ 100 day gap due to solar conjunction.
[5] The number of observations taken in that date range per filter.
[6] The total number of observations taken in that filter from all telescopes combined.

Table 3. The comparison stars AB magnitudes for each filter.

Filter	Comp 1	Comp 2	Comp 3	Comp 4	Comp 5
U	16.5 ± 0.2*	16.3 ± 0.2	17.5 ± 0.2	16.8 ± 0.2	17.6 ± 0.2
g'	15.737 ± 0.076*	14.994 ± 0.024	15.881 ± 0.081	15.071 ± 0.05	15.918 ± 0.049
V	15.388 ± 0.058	14.480 ± 0.019*	15.417 ± 0.035	14.449 ± 0.044	15.424 ± 0.031
r'	15.182 ± 0.047*	14.162 ± 0.063	14.962 ± 0.077	14.014 ± 0.041	15.110 ± 0.042
i'	14.89 ± 0.06	13.86 ± 0.04	14.58 ± 0.04*	13.54 ± 0.06	14.8 ± 0.1
z_s		13.7374 ± 0.0033*	14.4569 ± 0.0044	13.3687 ± 0.0005	14.6546 ± 0.0057

* Comparison stars used in the calibration.

high S/N, as well as numerous smaller features. These well-detected variations provide the basis for measuring inter-band time delays. We also note that there may be potential emission-line contamination of the broad-band photometric light curves, which could later impact on the measured time lags between the bands.

2.2 Spectroscopy

The spectroscopic observations were acquired robotically with the FLOYDS spectrographs between 2017 March and

2018 March. The FLOYDS spectrographs are two almost identical spectrographs on the LCO 2m telescopes, the Faulkes Telescope North (FTN) at Haleakela, Hawaii, and South (FTS) at Siding Springs in Australia. The spectrographs cover concurrently a wavelength range of $4800 - 10000$Å in first order and $3200 - 5900$Å in second order. The pixel scales are 3.51 Å/pixel in first order and 1.74 Å/pixel in second order, which corresponds to resolutions of 17Å and 9Å using a slit width of 2 arcseconds, respectively. For brevity, these will be referred to as the red and blue side respectively. We acquired a total of 149 spectroscopic epochs
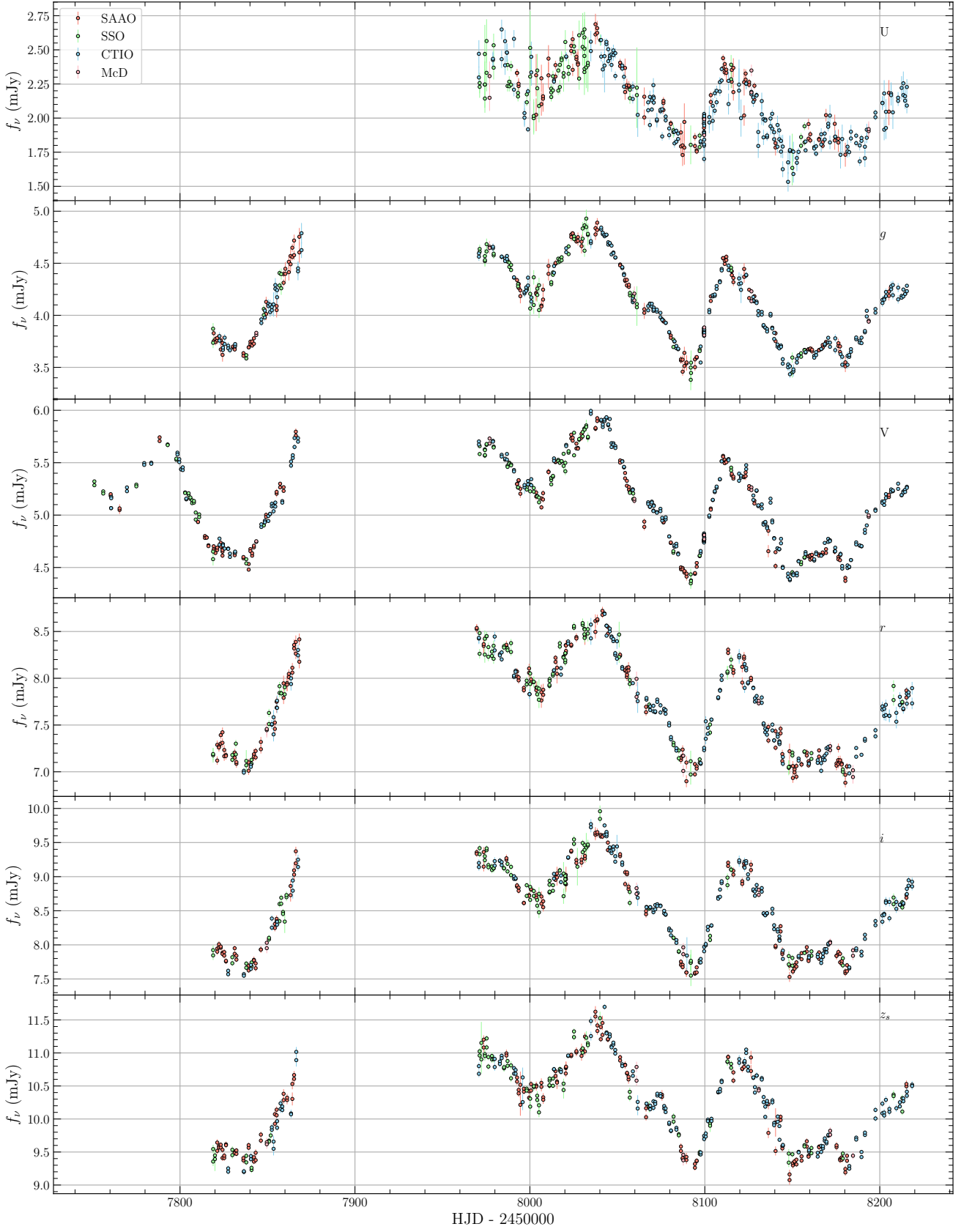
Figure 2. The 3C 120 continuum light curves in (top to bottom) U, g', V, r', i', z_s. Data are ordered by wavelength.

at a median sampling of 2 days. Spectra were taken in pairs with 1800 s per spectrum.

The data were reduced separately for the blue and red sides using the AGN FLOYDS pipeline written in PyRAF/Python[1]. The pipeline includes overscan subtraction, flat fielding, defringing, cosmic-ray rejection using the L.A.Cosmic algorithm (van Dokkum 2001), order rectification, spectral extraction, flux and wavelength calibration. All these steps were performed without human interaction.

We inspected the resulting 1-D spectra visually and we discarded the bad spectra, either due to significantly poor signal to noise or the pipeline failing to extract the 1-D spectra. Doing this procedure, we ended up with 128 blue spectra (97 FTN, 31 FTS) and 137 red spectra (98 FTN, 39 FTS). Since the Hβ emission line is observed in both orders (red and blue), it permits for simultaneous measurements of the line providing a way to cross check our measurements (Valenti et al. 2015).

We analysed separately the blue and red spectra, and further divided the FTN and FTS spectra, which have slightly different wavelength scales and flux calibrations. We also exclude the Hα line from further analysis as it is affected by fringing.

2.3 Spectral modeling with PrepSpec

To extract the emission-line light curves, we employ a multi-epoch spectral fitting tool called PrepSpec (Shen et al. 2015, 2016). PrepSpec was written in Fortran by K. Horne and is optimized to perform simultaneous spectral fitting of AGN spectra. We analyse spectra from the blue and red side separately. For a full description of PrepSpec, see Shen et al. (2016).

To mitigate flux calibration errors due to slit losses and changes in atmospheric transparency, PrepSpec fits a model to the input spectra defined as

$$\mu(t, \lambda) = p(t)[A(\lambda) + B(t, \lambda) + C(t, \lambda)], \qquad (2)$$

where $A(\lambda)$ is the average spectrum, $B(t, \lambda)$ is the variable BLR and $C(t, \lambda)$ is the variable continuum. $p(t)$ are the time-dependent photometric corrections determined by assuming that the narrow emission-line ([O III]$\lambda4959, 5007$ and other) fluxes remain constant throughout the RM monitoring period. Even though narrow emission-lines have been found to vary over long timescales (~several years, Peterson et al. 2013), this assumption is valid for short timescales (days to months). The variable BLR is modeled as a sum over lines of the line profile multiplied by the line light curve,

$$B(t, \lambda) = \sum_{\ell=1}^{N_\ell} B_\ell(\lambda) L_\ell(t). \qquad (3)$$

Here $\langle L \rangle = 0$ and $\langle L^2 \rangle = 1$ to resolve the degeneracy between $B_\ell(\lambda)$ and $L_\ell(t)$, so that the rms profile of the line ℓ is $B_\ell(\lambda)$. The light curve of the line ℓ is $L_\ell(t)$ multiplied by the integral of the line flux in the rms spectrum

$$B_\ell(t) = L_\ell(t) \int B_\ell(\lambda) \, d\lambda. \qquad (4)$$

---

[1] https://github.com/svalenti/FLOYDS_pipeline.git

The average spectrum $A(\lambda)$ is the sum of the broad-line, continuum and narrow-line components. Mathematically,

$$A(\lambda) = \bar{F}(\lambda) + N(\lambda). \qquad (5)$$

In this case $\bar{F}(\lambda)$ encapsulates both the broad-line and continuum components, and $N(\lambda)$ is the narrow-line component. Unlike many RM studies in which a power-law is used to model the changes in the continuum, PrepSpec uses a low-order polynomial in $\log \lambda$ with time-dependent coefficients to model the variations in the continuum $C(t, \lambda)$. PrepSpec also includes small corrections taking into account spectral blurring due to seeing and small wavelength shifts due to instrument flexure and differential refraction.

PrepSpec optimises the model parameters to fit all spectra simultaneously. PrepSpec outputs the mean and root-mean-square (rms) residual line profiles (Figure 3). The mean spectra exhibit strong narrow [OIII] emission-lines, with weaker narrow-line components on the Hγ, Hβ, He II $\lambda4686$, He I $\lambda5876$ lines. The PrepSpec model uses all of these narrow features to define the calibration tweaks. The blue and red spectra both cover Hβ and [OIII], providing two independent measures of the Hβ line profile and variations. The continuum is roughly flat in the mean f_λ spectrum and significantly bluer in the rms spectrum. The broad emission-lines are more prominent in the rms than in the mean spectrum, particularly for He II $\lambda4686$.

PrepSpec also produces measurements of the integrated broad emission-line fluxes (Figure 4), linewidth measurements (FWHM, σ_{line}) and their statistical errors for each of the broad-lines. The measured linewidths are listed in Table 4 for comparison. The highly ionized He II $\lambda4686$ line exhibits broader linewidth in the rms spectrum due to its close origin to the ionizing source. Generally, we measure small uncertainties on the linewidths due to high S/N of our data. However, we do note that because of the ambiguity in separating the NLR and BLR components, and placing the continuum, the measured linewidths may be over/under estimated.

Correlated variations across all the emission-lines are seen in Figure 4. The He II $\lambda4686$ variations track the V-band variations quite closely, while He I $\lambda5876$ and the Balmer line variations exhibit evidence for a more substantial lag, despite their relatively large scatter around HJD-2450000 = 8100-8150. For example, the V-band light curve rises from 8090-8110 and then falls until 8150. In this same time interval He II rises and falls similarly to V while the Balmer and He I rise and flatten off. Near 8020-8030 the He II $\lambda4686$, He I $\lambda5876$ and Balmer line fluxes seem low compared with the relatively high V-band flux. This suggests that long-term trends may differ between lines and continuum, thus potentially affecting lag measurements based on the faster variations.

3 TIME-SERIES ANALYSIS

3.1 Variability Amplitudes

We characterize the variability of each light curve by measuring the fractional rms amplitude, F_{var}, defined as

$$F_{\text{var}} = \frac{\sqrt{\sigma_\ell^2 - \delta_{\text{rms}}^2}}{\langle \ell \rangle}, \qquad (6)$$

Table 4. Emission-line widths in the Mean and RMS spectra.

Line	FWHM(mean) (km s^{-1})	FWHM(rms) (km s^{-1})	σ_{line}(mean) (km s^{-1})	σ_{line}(rms) (km s^{-1})	Window (Å)
Hγ	4402 ± 5	4469 ± 14	1703 ± 1	1786 ± 3	$4270 - 4415$
He II $\lambda 4686$	5271 ± 20	6592 ± 26	2007 ± 4	2282 ± 2	$4609 - 4766$
Hβ blue side	4754 ± 4	3273 ± 8	1923 ± 1	1657 ± 3	$4782 - 4944$
Hβ red side	4412 ± 5	3874 ± 12	2002 ± 1	1810 ± 3	$4782 - 4944$
He I $\lambda 5876$	3948 ± 11	4408 ± 30	2044 ± 4	2037 ± 12	$5751 - 6006$

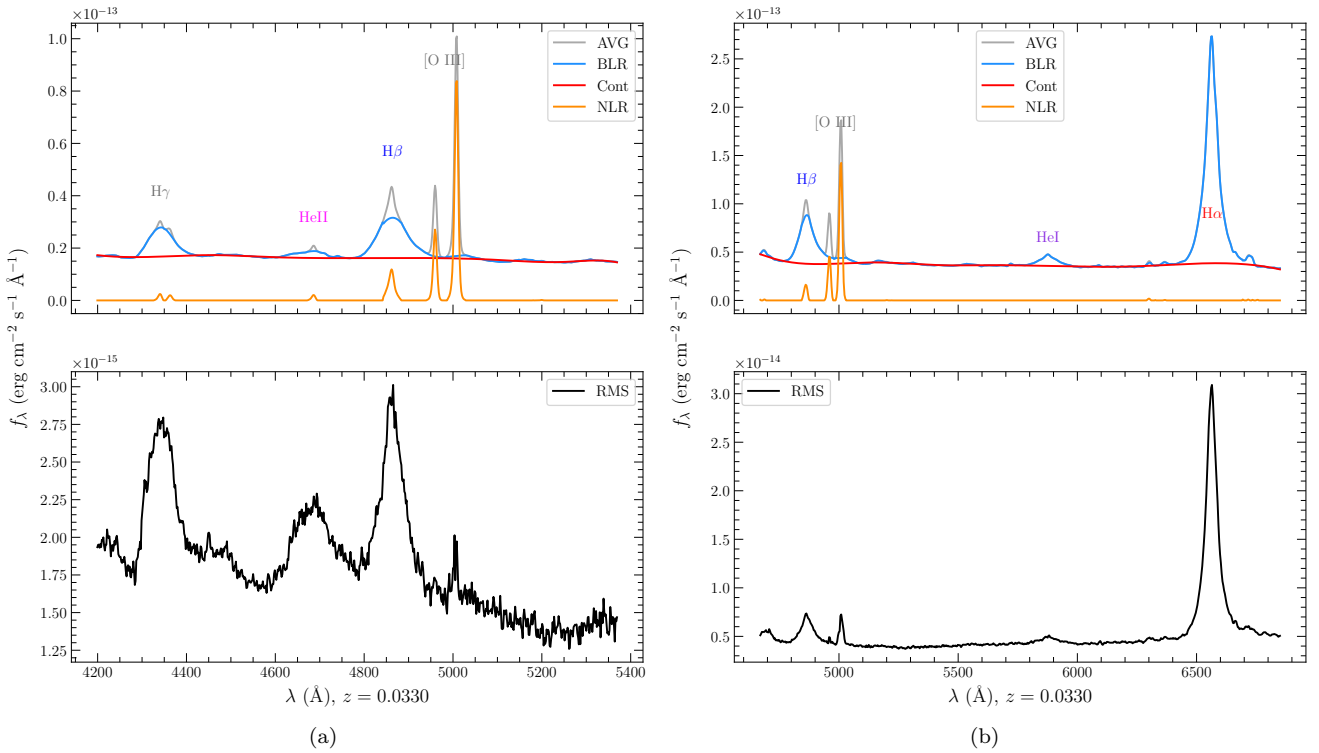**Figure 3.** (Left) Mean (top) and rms (bottom) spectrum of 3C 120 from FTN data (blue-side), which includes 97 epochs. Labeled are Hγ $\lambda 4340$, He II $\lambda 4686$, Hβ $\lambda 4861$ and [O III] $\lambda\lambda 4959, 5007$ emission-lines. (Right) Mean (top) and rms (bottom) spectrum of 3C 120 from FTN data (red-side), which includes 98 epochs. Labeled are Hβ $\lambda 4861$, [O III] $\lambda\lambda 4959, 5007$, and He I $\lambda 5876$ emission-lines. The Hα line is excluded from our time-series analysis due to it being affected by fringing.

where $\langle \ell \rangle$ and σ_{ℓ}^2 are the mean and variance of the light curve, the δ_{rms}^2 is the rms uncertainty on the measured fluxes (Rodríguez-Pascual et al. 1997; Edelson et al. 2002). The calculated F_{var} and its uncertainty for each broad emission-line light curve are tabulated in Table 5. The variability amplitude of about 10% is considered adequate for reverberation studies (Rodríguez-Pascual et al. 1997). He II $\lambda 4686$ exhibits substantial (30% rms) variability. Correlated variations are evident in the Balmer and He I lightcurves despite their lower fractional variations ($\sim 8 - 11\%$). We also calculate F_{var} for the continuum light curves (Figure 2) and list the results in Table 7. We generally find F_{var} values that decrease with increasing wavelength likely due to the variable com-

ponent of the light from the accretion disc being bluer than the non-variable components, such as host galaxy starlight with the exception of i' band.

3.2 Cross-Correlation Analysis

To estimate the time delay τ of the broad emission-lines (Hγ, He II, Hβ, He I) relative to the continuum light curve, we used the interpolation cross-correlation function (ICCF, Gaskell & Sparke 1986; Gaskell & Peterson 1987; White & Peterson 1994) method. We cross-correlated the emission-line light curves (Figure 4) with the V-band continuum light curve (Figure 2). We chose the V-band continuum light curve
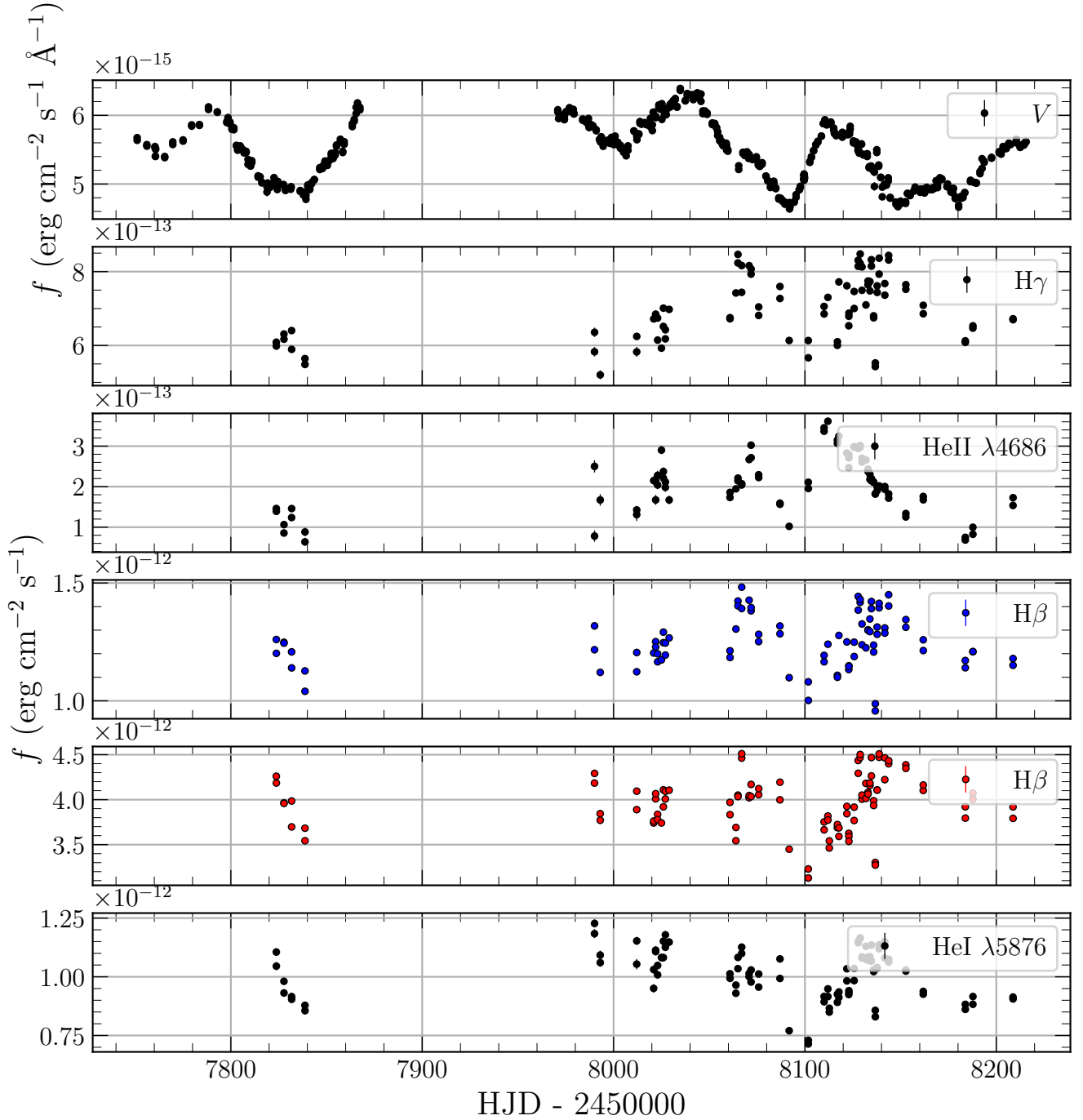
Figure 4. V-band continuum and broad emission-line (Hγ λ4340, He II λ4686, Hβ λ4861, He I λ5876) light curves from PrepSpec using FTN data.

because it has more observations and better signal-to-noise than the other continuum light curves in Figure 2.

For two light curves $x(t)$ and $y(t)$ sampled at times t_i, the cross-correlation function ICCF (τ) is given by

$$\text{ICCF}(\tau) = \frac{1}{N} \frac{\sum_i (x(t_i) - \bar{x})(y(t_i - \tau) - \bar{y})}{\sigma_y \sigma_x}, \qquad (7)$$

where $\bar{x}$ and σ_x are the mean and standard deviation of the N lightcurve samples $x(t_i)$, and similarly for y. In the

ICCF, the cross-correlation coefficient is calculated twice. Firstly, by cross-correlating the original continuum light curve $y(t_i)$ with the linearly interpolated emission-line light curve $x(t_i - \tau)$ for a given lag τ. Secondly, by cross-correlating the linearly interpolated continuum light curve $y(t_i - \tau)$ with the original emission-line light curve $x(t_i)$ for a given lag. The ICCF (τ) is then taken to be the mean of the two results. We explored a time lag range from −10 to 50 days using

Table 5. 3C 120 broad emission-line lags relative to V.

Line Curve	r_{max}	τ_{cent} (days)	$\tau_{CREAM} - \tau_V$ (days)	F_{var}
Hγ	0.28	$18.8^{+1.3}_{-1.0}$	17.6 ± 1.3	0.110 ± 0.008
He II	0.53	$2.7^{+0.7}_{-0.8}$	3.0 ± 0.7	0.296 ± 0.022
Hβ blue-side	0.42	$21.2^{+1.6}_{-1.0}$	19.4 ± 1.7	0.083 ± 0.006
Hβ red-side	0.38	$21.2^{+1.6}_{-1.0}$	20.2 ± 2.4	0.089 ± 0.006
He I	0.69	$16.9^{+0.9}_{-1.1}$	16.6 ± 1.3	0.102 ± 0.007

$\tau_V = 2.26 \pm 0.18$ days

the interpolation grid spacing of 0.25 days. We based our measured lags on the ICCF centroid (τ_{cen}) calculated using all r values above a threshold $r > 0.8r_{max}$ (Peterson et al. 2004), where r_{max} is the maximum value of the correlation coefficient.

Uncertainties on the measured lags were determined using the flux randomization and random subset selection method (FR/RSS, Peterson et al. 1998a) in the form of Py-CCF[2](Sun et al. 2018). For each realization or iteration, individual points are sampled randomly from the original set with replacement, thus resulting in some of the points being excluded and others being selected more than once. In the resulting set, the duplicate points are ignored, which then reduces the set to typically $\sim 37\%$ of the original set. The remaining points are then perturbed by adding random Gaussian deviates based on the associated error and each time calculating τ_{cen}. This procedure was repeated 10^3 times to build up a cross-correlation centroid distribution (CCCD, Figure 5) which yielded the median lag and the 68% confidence interval.

In our ICCF analysis, we omit the FTS data. When using both FTS and FTN spectra, which have slightly different wavelength scales and flux calibrations, the resulting merged emission-line lightcurves had small but significant jumps between the FTN and FTS data points. This adversely affected the ICCF analysis. Therefore we opted to use just the FTN spectra, which had better time sampling than FTS. We summarise the resulting ICCF lag measurements in Table 5 (and Figure 5). The FTN blue and red spectra give consistent Hβ lag measurements with $21.2^{+1.6}_{-1.0}$ and $21.2^{+1.6}_{-1.0}$ days respectively, indicating that our emission-line flux measurements are reliable. The Hγ lag ($18.8^{+1.3}_{-1.0}$) is consistent with the Hβ measurements. The He lines, He II $\lambda4686$ lag ($2.7^{+0.7}_{-0.8}$) and He I $\lambda5876$ lag ($16.9^{+0.9}_{-1.1}$) have shorter delays than the Balmer lines. Generally, we measure r_{max} values that are lower for each of the broad lines despite the ICCF being well-behaved. 3C 120 being a radio-galaxy (also a miniblazar), there may be an additional contribution by the optical synchrotron continuum emission from the jet which could affect the correlation coefficient values (Li et al. 2019; Zhang et al. 2019). However, synchrotron emission would introduce features in the continuum light

curve, and the low correlation coefficients we see stem from relatively large scatter in the emission-line (particularly Hγ and Hβ) data that are not present in the V continuum light curve. We believe this scatter arises from limitations in the accuracy of our spectrophotometric calibration, rather than to variable jet emission affecting the light curves. To try to improve the coefficients, we applied detrending (Welsh 1999) prior to ICCF analysis. We then omitted the pre-gap spectra with/without detrending. In all cases, the ICCF results did not improve considerably.

In addition to the broad emission-line lags with ICCF, we measure the lag between the continuum bands with respect to V in a similar manner as above (Table 7). We give more emphasis on the outcome and implications in terms of the standard disc model in Section 4.

3.3 CREAM Modelling

We undertook a separate analysis of the light curves in addition to the ICCF, using the Continuum REprocessed AGN Markov Chain Monte Carlo code (CREAM, Starkey et al. 2016)[3] with the aim of comparing the results with the ICCF. The ICCF method works best with regularly-sampled data and accurate uncertainty estimates, while CREAM fits a parameterised model to the lightcurve data, including parameters for the reverberating disc model and a noise model, with 1 or 2 parameters per lightcurve that adjusts the nominal error bars. The noise model optimizes an additive extra variance parameter (σ_0^2) and multiplicative error-bar scaling factor (e) such that

$$\sigma_{new} = \sqrt{(e\sigma_{old})^2 + \sigma_0^2} \,. \tag{8}$$

For the CREAM analysis, we model both FTN and FTS data simultaneously. CREAM fits a lamppost model with driving light curve $X(t)$ to the input continuum light curves $f_\nu(\lambda, t)$ with the continuum response function $\psi(\tau|\lambda)$,

$$f_\nu(\lambda, t) = \bar{F}_\nu(\lambda) + \Delta F_\nu(\lambda) \int X(t - \tau)\psi(\tau|\lambda)d\tau \,, \tag{9}$$

in order to infer the shape of the true driving light curve that drives the continuum variability. The driving lightcurve $X(t)$ is normalised to $\langle X \rangle = 0$ and $\langle X^2 \rangle = 1$, so that $\bar{F}_\nu(\lambda)$ and $\Delta F_\nu(\lambda)$ represent the mean and rms spectra respectively. The continuum response function is normalised to $\int \psi(\tau|\lambda)d\tau = 1$. For the continuum delay distribution, we adopt a face-on (inclination $i = 0$) steady-state blackbody accretion disc with a power-law temperature profile

$$T = T_1 \left(\frac{r}{r_1}\right)^{-\alpha} \,, \tag{10}$$

where T_1 is the temperature at $r_1 = 1$ light day, and $T \propto r^{-\alpha}$ corresponds to $\tau \propto \lambda^{1/\alpha}$. For the steady disc model, $\alpha = 3/4$ and $\tau \propto \lambda^{4/3}$ and

$$T_1^4 = \frac{3\,G\,M\,\dot{M}}{8\,\pi\,\sigma\,r_1^3} \,, \tag{11}$$

for a given black hole mass M and mass accretion rate $\dot{M}$. Thus $\tau(\lambda)$ tests the prediction $\alpha = 3/4$ and T_1 then measures the product $M\dot{M}$.

---

[2] https://bitbucket.org/cgrier/python_ccf_code

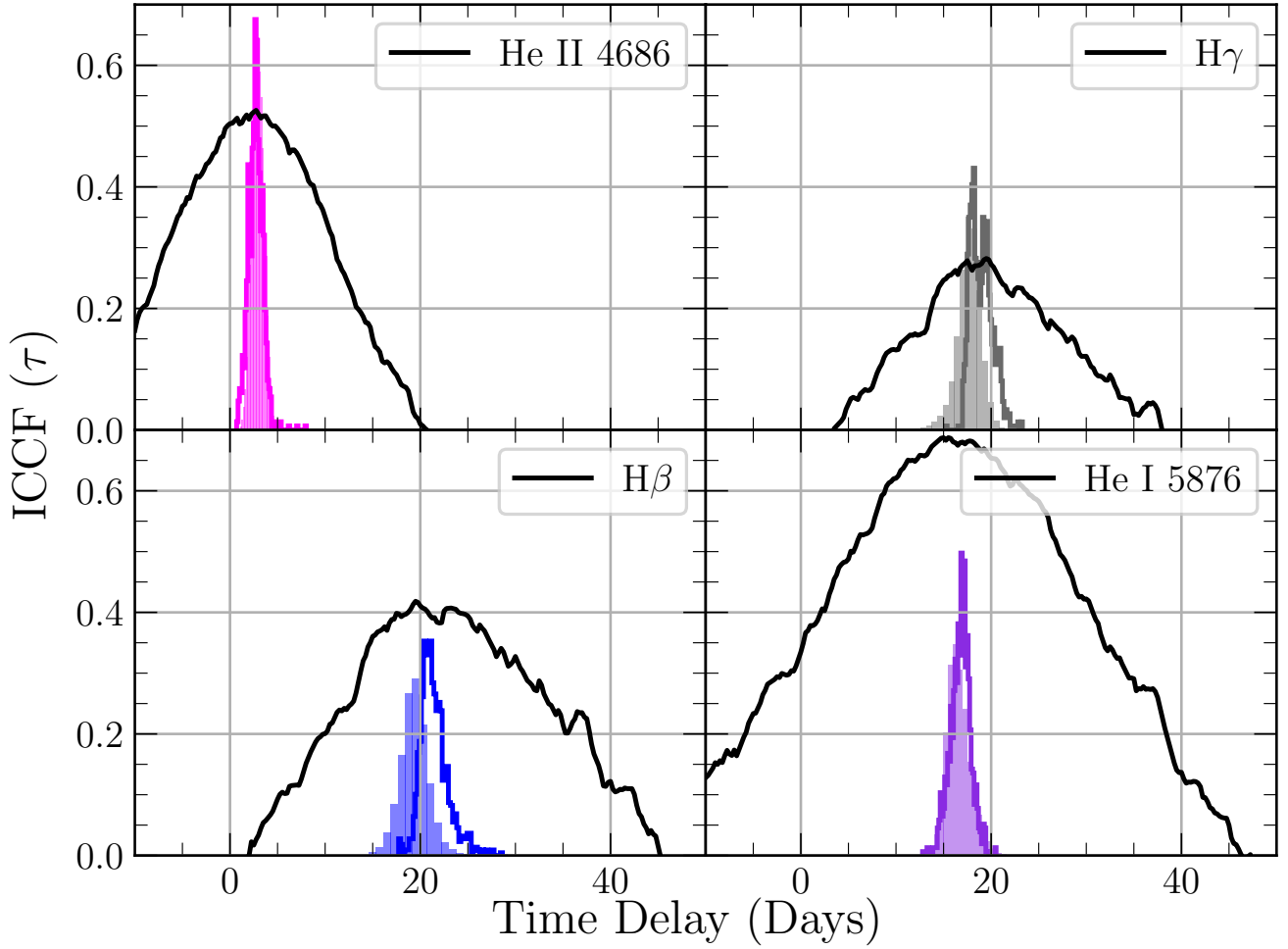[3] Python version from https://github.com/dstarkey23/pycecream

Figure 5. The solid lines are the ICCFs $r(\tau)$, and corresponding cross-correlation centroid distributions (CCCD) defined by the FR/RSS samples (solid lines histograms). The translucent histograms are the posterior delay distributions (also shown in Figure 7 panels a-e, defined by CREAM's MCMC samples of the mean delay of top-hat response functions. These results are for FTN spectra only.

CREAM assumes the origin of accretion disc variability is a centrally located point source with a stochastic luminosity modelled as a time series $X(t)$ given by

$$X(t) = \sum_{k=1}^{N_k} C_k \cos(\omega_k t) + S_k \sin(\omega_k t), \quad (12)$$

where $\omega_k \equiv k \, \Delta\omega$ are equally-spaced fourier frequencies, with C_k and S_k the corresponding fourier amplitudes that describe the shape of the lamppost light curve variations. To incorporate prior knowledge about the character of AGN lighcurves, CREAM includes priors on the S_k and C_k parameters that steer the power spectrum of the driving light curve toward a random walk, with fourier power-density spectrum $P(\omega) \propto \omega^{-2}$. These random walk priors are gaussian with mean $\langle S_k \rangle = \langle C_k \rangle = 0$ and standard deviation σ_k, where

$$\sigma_k^2 = \langle S_k^2 \rangle + \langle C_k^2 \rangle = P(\omega_k) \, \Delta\omega = P_0 \, \Delta\omega \left(\frac{\omega_0}{\omega_k} \right)^2 . \quad (13)$$

CREAM's fitted parameters and their priors are summarized in Table 6.

Following Grier et al. (2017b) we use CREAM to fit

Table 6. Summary of priors on each of the CREAM parameters.

Parameter	N_{par}	Prior
S_k and C_k	$2N_k$	Gaussian ($\langle S_k \rangle = \langle C_k \rangle = 0$, $\langle S_k^2 \rangle = \langle C_k^2 \rangle = \sigma_k^2$)[a]
i	0	0
T_1	1	Log Uniform
α	0	3/4
$\Delta F_\nu(\lambda)$	$N_\lambda \times N_{\text{telescopes}}$	Log Uniform
$\overline{F}_\nu(\lambda)$	$N_\lambda \times N_{\text{telescopes}}$	Log Uniform
$\bar{\tau}(\lambda)$[b]	N_λ	Uniform

[a] σ_k is defined in Equation 13.
[b] The top-hat centroid lag parameter is optional and used as a substitute for CREAM's disc response function parameters T_1, α, and i if CREAM is run in 'top-hat' mode.

multiple continuum lightcurves simultaneously with multiple emission-line lightcurves. For each line we adopt a uniform (top hat) delay distribution specified by mean delay $\bar{\tau}$

Table 7. 3C 120 continuum lags relative to V in the observed frame.

Line Curve	λ (Å)	$\tau_{\rm cent}$ (days)	$\tau_{\rm CREAM} - \tau_{\rm V}$ (days)	$F_{\rm var}$
U	3656	$0.14^{+0.35}_{-0.36}$	-0.94 ± 0.21	0.114 ± 0.005
g'	4770	$-0.63^{+0.13}_{-0.13}$	-0.38 ± 0.24	0.092 ± 0.003
V	5477	$0.00^{+0.13}_{-0.12}$	0.00 ± 0.26	0.080 ± 0.002
r'	6231	$1.50^{+0.24}_{-0.24}$	0.42 ± 0.28	0.060 ± 0.002
i'	7625	$2.60^{+0.24}_{-0.24}$	1.25 ± 0.34	0.070 ± 0.002
z_s	8660	$2.86^{+0.24}_{-0.24}$	1.9 ± 0.4	0.059 ± 0.002

$\tau_{\rm V} = 2.26 \pm 0.18$ days

and delay width $\Delta\tau$. This is based on the assumption that the BLR responds to changes by the driving light curve. CREAM treats the emission-line light curves as delayed and smoothed versions of the inferred driving light curve with a top hat response function similar to that used in JAVELIN (Zu et al. 2011). CREAM estimates parameter uncertainties using a Markov chain, in our case with 10^5 samples.

In modelling the light curves, we fit only the temperature T_1 at 1 light day from the black hole, holding the power-law index $\alpha \equiv 3/4$ and face-on inclination $i = 0$. We used our derived black hole mass $M = 6.3 \times 10^7\,{\rm M_\odot}$ (Section 5) for consistency. We also set the upper frequency limit to 0.5 cycles per day for the driving light curve, the width of the top hat response to 2 days and restricted the time delay to be within -10 to 50 days. The CREAM fits to the continuum and line light curves are shown in Figures 6-7, along with the inferred driving light curve. The model yielded a fit that is a reasonable representation of most of the observed features in the light curves with a few exceptions here and there. The U-band light curve, Figure 6 (panel h), exhibits large error bars due to atmospheric extinction.

The measured lags and their uncertainties are shown in Table 5 and Table 7, relative to V-band in the observed frame. Since we are measuring relative to V-band, we therefore need to subtract this continuum lag from other CREAM values in order to compare CREAM lags to those obtained with the ICCF method. We find that the two methods give consistent results to within uncertainties for Hγ, He II λ4686, He I λ5876 and Hβ lags. We interpret the continuum lags obtained with both ICCF and CREAM in terms of the accretion thin-disc model in Section 4.

4   INTER-BAND CONTINUUM LAGS

We investigate the accretion disc structure in 3C 120 in terms of the standard accretion disc model (Shakura & Sunyaev 1973). In this model, continuum delays increase with increasing wavelength due to thermal reprocessing, where the hotter inner part of the disc responds to the variable ionizing source before the cooler outer part of the disc. The lag is interpreted as the light-travel time from the ioniz-

Table 8. CREAM model best-fit parameters.

Parameter	Value
T_1 ($10^4 K$)	1.51 ± 0.10
i (deg)	0
α	0.75

Table 9. Mean and rms Spectra from CREAM.

λ (Å)	$\overline{F}_\nu(\lambda)$ (mJy)	$\Delta F_\nu(\lambda)$ (mJy)
3656	7.604 ± 0.011	0.937 ± 0.013
4770	11.308 ± 0.009	0.96 ± 0.01
5477	11.80 ± 0.01	0.92 ± 0.01
6231	15.516 ± 0.013	0.929 ± 0.013
7625	14.317 ± 0.015	0.890 ± 0.013
8660	15.442 ± 0.016	0.817 ± 0.015

The dust-extinction-corrected values.

ing source to the reprocessing site, where it is reprocessed into UV/Optical continuum emission. The temperature profile of the accretion disc changes with radius $r = c\tau$ as $T(r) \propto r^{-3/4}$, for a given black hole mass M and accretion rate $\dot{M}$. The wavelength-dependent lags have been detected before in several studies across a wide range of continuum bands (e.g. Cackett et al. 2007; Edelson et al. 2015; Fausnaugh et al. 2016, 2018; Jiang et al. 2017) with statistically significant lag detections, as predicted by the reprocessing model. We use CREAM as described in Section 3.3 to fit a steady-state blackbody disc model to the U, g', V, r', i', z_s continuum light curves, in order to assess the temperature profile of the disc $T(r)$ in 3C 120, and determine the accretion rate $\dot{M}$ for $M = 6.3 \times 10^7\,{\rm M_\odot}$. The resulting CREAM model best-fit parameters are presented in Table 8 and 9. The probability distribution for T_1 is shown in Figure 8, yielding the best fit value of $T_1 = (1.51 \pm 0.10) \times 10^4$ K. This value of T_1 corresponds to $\dot{M} = 0.60 \pm 0.15\,M_\odot{\rm yr}^{-1}$ (Eqn. 11) for our measured BH mass $M = 6.3 \times 10^7\,{\rm M_\odot}$, giving $\log(M\dot{M}/{\rm M_\odot^2 yr}^{-1}) = 7.58 \pm 0.11$. We also report an Eddington ratio $\dot{m}_{\rm Edd} = \dot{M}/\dot{M}_{\rm Edd} = L/L_{\rm Edd} = 0.42^{+0.10}_{-0.09}$. The ratio $L/L_{\rm Edd}$ is influenced by, (1) the inclination and (2) the adopted BH mass which is uncertain by 0.4 dex.

4.1   Lag spectrum

We present the CREAM mean delays alongside ICCF measurements for comparison in Table 7, and plotted in Figure 9. The CREAM lags increase as $\lambda^{4/3}$ since the CREAM model assumes a flat blackbody disc with $T \propto R^{-3/4}$. The ICCF results also show the same trend of rising lag with wavelength, with the exception of the U-band. The U-band resulted in a longer lag than would be expected (i.e. larger than the lag between V and g'). This enhanced U lag has been encountered before (e.g., Edelson et al. 2015; Fausnaugh et al. 2016) and is said to be due to the considerable contribution of Balmer continuum and high-order Balmer lines in the U-band.

The observed delay spectrum $\tau(\lambda)$ tests the accretion

Table 10. Lag Spectrum Parameter Fits

Wavelength	τ_0	β	χ^2/dof	dof
All	3.51 ± 0.22	$4/3$	8.44	4
	2.42 ± 1.11	1.79 ± 0.62	10.95	3

disc theory. A thin steady-state blackbody accretion disc has $T^4 = 3\,G\,M\,\dot{M}/8\,\pi\,\sigma\,r^3$ and thus with $T \propto h\,c/k\,\lambda$ for blackbody emission, the predicted delay spectrum should follow $\tau = r/c \propto (M\,\dot{M})^{1/3}\,\lambda^{4/3}$ (Shakura & Sunyaev 1973). More generally, $\tau \propto \lambda^\beta$ corresponds to $T \propto r^{1/\beta}$.

To quantify the lags for a disc reprocessing model, we fit the ICCF lags with a power law of the form

$$\tau(\lambda) = \tau_0 \left[(\lambda/\lambda_0)^\beta - 1 \right], \qquad (14)$$

where λ_0 is the reference wavelength, β is the power-law index which corresponds to the temperature-radius slope $T \propto r^{-\alpha}$ where $\alpha = 1/\beta$ and τ_0 is a normalization factor for measuring the radius of the disc at λ_0. In Figure 9, the orange and black curves show fits of this model with $\lambda_0 = 5477\text{Å}$ and β fixed at $4/3$ (black) and free to vary (orange). Since there is an error bar on the ICCF V-band lag ($0.00^{+0.13}_{-0.12}$ days), we add a wavelength-independent constant parameter to Eqn. 14. This new parameter allows for non-zero V-band lag, in other words we do not force the fit to have zero lag at V-band wavelength. In doing so, we find best-fit value of $\tau_0 = 3.51 \pm 0.22$ days from ICCF ($\chi^2/\mathrm{dof} = 8.44$ for dof $= 4$). When β is allowed to vary, we find values of $\tau_0 = 2.42 \pm 1.11$ days and $\beta = 1.79 \pm 0.62$ from ICCF measurements ($\chi^2/\mathrm{dof} = 10.95$ for dof $= 3$), see Table 10. Therefore, we discuss the results for fixed $\beta = 4/3$.

We find that the function gives a poor fit to the ICCF lags owing to the excessive U-band lag and potentially excessive r' and i' lags as well. The large ICCF lags are evident from Figure 9, with lags of i', z_s being comparable to and larger than that of the high-ionization-state lines such as He II $\lambda 4686$. Comparing the intercepts to infer the radius of the disc at λ_0, $\tau_0 = 3.51 \pm 0.22$ days for ICCF lags versus $\tau_0 = 2.26 \pm 0.18$ days for CREAM, implies a radius that is a factor of 1.55 ± 0.16 times larger than would be expected from the standard thin-disc model. This discrepancy could be due to several different sources: (1) difficulties in the ICCF in measuring the lags due to slightly noisier U light curve (SNR $= 50$), influence by outliers, or over influenced by the observing gap, (2) contamination of the disc continuum emission by HI bound-free continuum emission from the BLR (Korista & Goad 2001; Lawther et al. 2018; Chelouche et al. 2019; Korista & Goad 2019). This produces a composite delay distribution, with a sharp peak at small lags from the disc continuum, and a broader peak with longer delays from the BLR. Evidence for this HI bound-free continuum from BLR is shown by the Balmer jump at 3640Å and Paschen jump at 8200Å in the ICCF lag spectrum. We do not account for diffuse continuum contribution to the measured continuum lags, we leave that here for future work.

4.1.1 Accretion-disc Spectrum

The linearised reprocessing model assumes that continuum variations respond linearly to the lamppost with a time delay that depends on light-travel time effects. We see from the CREAM fit shown in Figure 6 that an approximate linear relation exists between the inferred driver and disc light curves (both experience correlated variations). We explore this further in Figure 10. The response light curves are plotted relative to the driving light curve $X(t - \tau)$, averaged over the time delay distribution $\Psi(\tau)$ to demonstrate this linear relation. Figure 10 shows that this relation holds across all continuum bands indicating that, despite larger than expected delays, a linearised echo description is apparent from correlated variability of these light curves.

In Figure 11, we plot the rms disc spectrum (variable component of the light) derived from the CREAM fit slopes in Figure 10 and denoted as $\Delta F_\nu(\lambda)$ in Eqn. 9 and Table 9. The average (disc+galaxy) spectrum is derived from the CREAM fit intercepts in Figure 10 and denoted as $\overline{F}_\nu(\lambda)$. Also, shown is the $F_{\max}(\lambda) - F_{\min}(\lambda)$ spectrum corresponding to the difference between maximum and minimum observed fluxes for each wavelength. As a reference, we overplot the fiducial $f_\nu \propto \nu^{1/3}$ power-law disc spectrum (yellow). From the observed fluxes (dashed lines), it appears that the rms disc spectrum is red rather than blue. We attribute this to extinction and reddening by dust in the Milky Way (MW). We correct for MW extinction using a dust extinction map (Schlegel et al. 1998) with $E(B - V) = 0.29\,\mathrm{mag}$ and an extinction curve of Fitzpatrick (1999) with $R_V = 3.1$. After correcting for MW dust extinction (solid lines), we can see that the variable disc spectrum is blue and quite close to the $\nu^{1/3}$ spectrum predicted by the thin-disc theory, while the average (disc+galaxy) spectrum remains red. We note that there is no obvious sign in the dust-corrected $\Delta F_\nu(\lambda)$ or $F_{\max}(\lambda) - F_{\min}(\lambda)$ disc spectrum of Figure 11 of Balmer or Paschen jumps that might be expected given their signature in delay spectrum $\tau(\lambda)$ of Figure 9.

We next compare the predicted disc spectrum calculated from the $T(r)$ profile derived from the CREAM fit to $\tau(\lambda)$, with the observed disc spectrum flux. CREAM fit estimates $T(r)$ from $\tau(\lambda)$ (i.e. $M\dot{M}$ from Figure 8) and independently of that also estimates the disc flux $f_\nu(\lambda)$ at each wavelength. These are the $\Delta F_\nu(\lambda)$ and $\bar{F}_\nu(\lambda)$ in Eqn. 9, which are the slopes and intercepts respectively, plotted as a (MW-dust corrected) spectrum in Figure 11. We want to ascertain if the $T(r)$ from the $M\dot{M}$ in Figure 8 predicts a disc spectrum $f_\nu(\lambda)$ that is consistent with (or brighter than, or fainter than) the independently measured disc spectrum in Figure 11. We make use of Eqn. 4 in Cackett et al. (2007) and Eqn. 2 in Collier et al. (1999) to derive predicted spectra, and compare with the mean disc $\bar{F}_{\mathrm{disc}}$ spectrum (red) in Figure 12, where

$$\bar{F}_{\mathrm{disc}}(\lambda) = \bar{F}(\lambda) - F_{\mathrm{gal}}(\lambda), \qquad (15)$$

$$F_{\mathrm{gal}}(\lambda) = \bar{F}(\lambda) + X_{\mathrm{gal}}\Delta F(\lambda). \qquad (16)$$

It follows from Figure 12 that the predicted disc spectrum (for $i=0$) is brighter by a factor ~ 4 compared with the $\bar{F}_{\mathrm{disc}}$ spectrum. Also, the shape of the $\bar{F}_{\mathrm{disc}}$ spectrum is close to $f_\nu \propto \nu^{1/3}$, in agreement with predicted spectrum for a thin steady-state blackbody disc, but the surface brightness of the disc is lower by a factor ~ 4 compared with a face-on
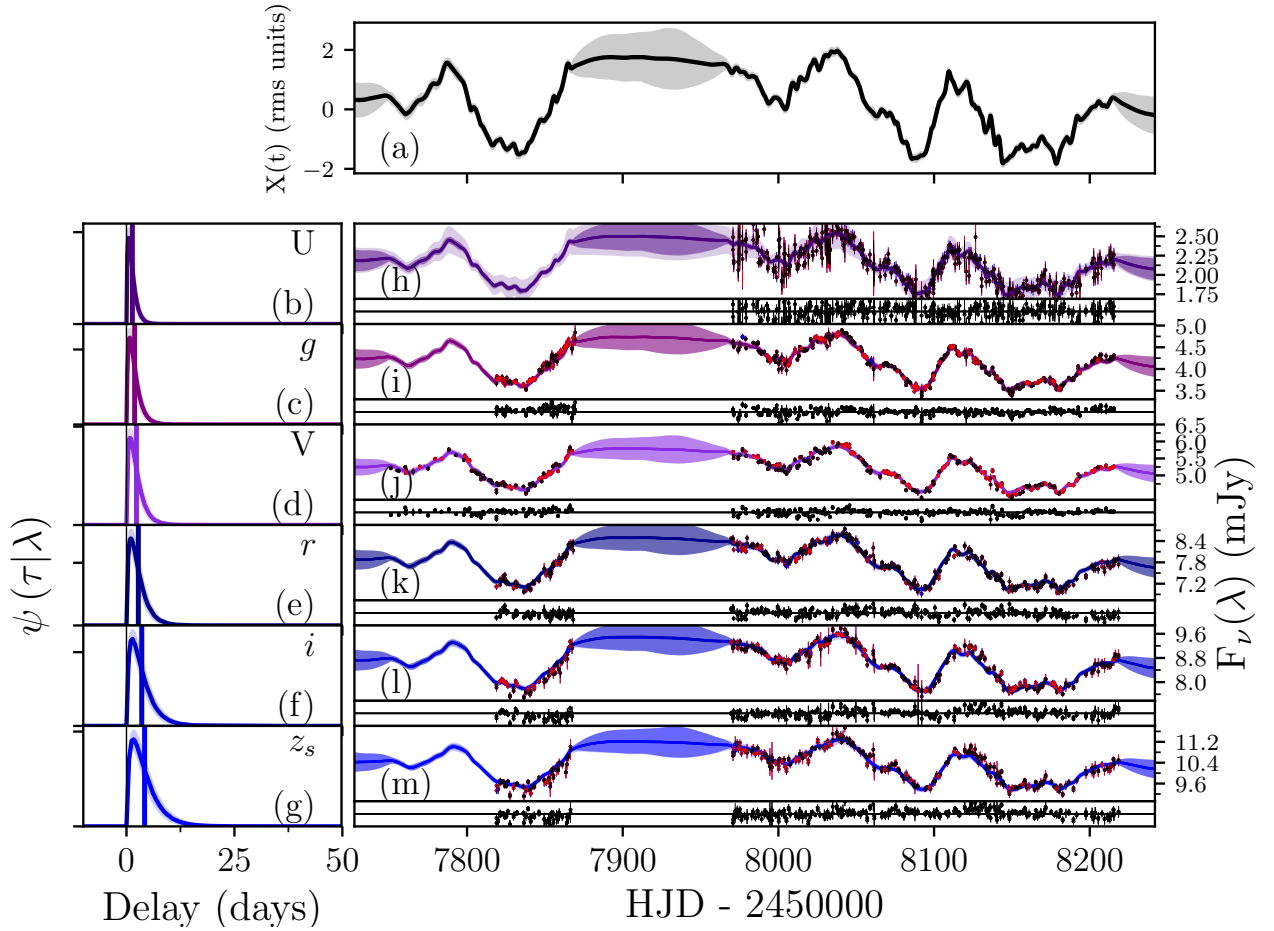
Figure 6. CREAM fits to the continuum light curves (panels h-m) from 3C 120. The upper figure (panel a) shows the inferred driving light curve. Panels b-g show the response functions where the vertical line denote the mean lags. Also, shown are the fit residuals in panels h-m. The red and blue are the rescaled error bars using Eqn. 8.

blackbody disc with the $T(r)$ profile derived from the delay spectrum $\tau(\lambda)$. This discrepancy is in the same direction as, and somewhat larger than, the result found by Starkey et al. (2017) for the disc in NGC 5548. It suggests that the effect may be more general and not just a peculiarity of NGC 5548.

4.1.2   Optical Luminosity at 5100Å

Using the flux-flux analysis method from CREAM, we determine the optical luminosity at 5100Å corresponding to our monitoring campaign. A linear relationship is observed between the CREAM inferred driving light curve (assuming that continuum variations are driven by a central source of irradiation) and all continuum bands. The best-fit mean flux $\bar{F}$ and rms flux ΔF for each wavelength are listed in Table 9, after correcting for galactic extinction following Schlegel et al. (1998). The total flux in each filter includes contributions from the disc and host galaxy. We quantify the galaxy's contribution by evaluating the linear trend lines at $X_{gal} = -8.12$ for each filter (Figure 10). The value X_{gal} is de-

fined to be the point where the linear fit extrapolated to low flux first crosses zero. This occurs first at $X_{gal} = -8.12$, for the fit to the shortest-wavelength U-band flux. Table 11 summarizes the results of decomposing total (disc+galaxy) flux into galaxy and disc (total-galaxy) components. We determine the interpolated host-galaxy flux at 5100Å of 3.913 ± 0.077 mJy.

Bentz et al. (2006) using high resolution HST images, determined the host-galaxy flux at 5100Å (5.22 mJy) after correcting for extinction and adding narrow-line contribution (Sakata et al. 2010). Bentz et al. (2009a) re-modeled the host-galaxy flux at 5100Å and found it to be 3.32 mJy. The difference between these two host-galaxy estimates is linked with the difference in the decomposition modeling techniques of the galaxy (Pozo Nuñez et al. 2012). Through interpolating, we determine the disc (total-galaxy) flux at 5100Å to be $f_{obs}[5100(1 + z)] = 7.55 \pm 0.08$ mJy. Using the redshift distance of 139 Mpc, we measure the luminosity at the time of our campaign to be $(9.94 \pm 0.11) \times 10^{43}$ erg s^{-1} (Table 12).
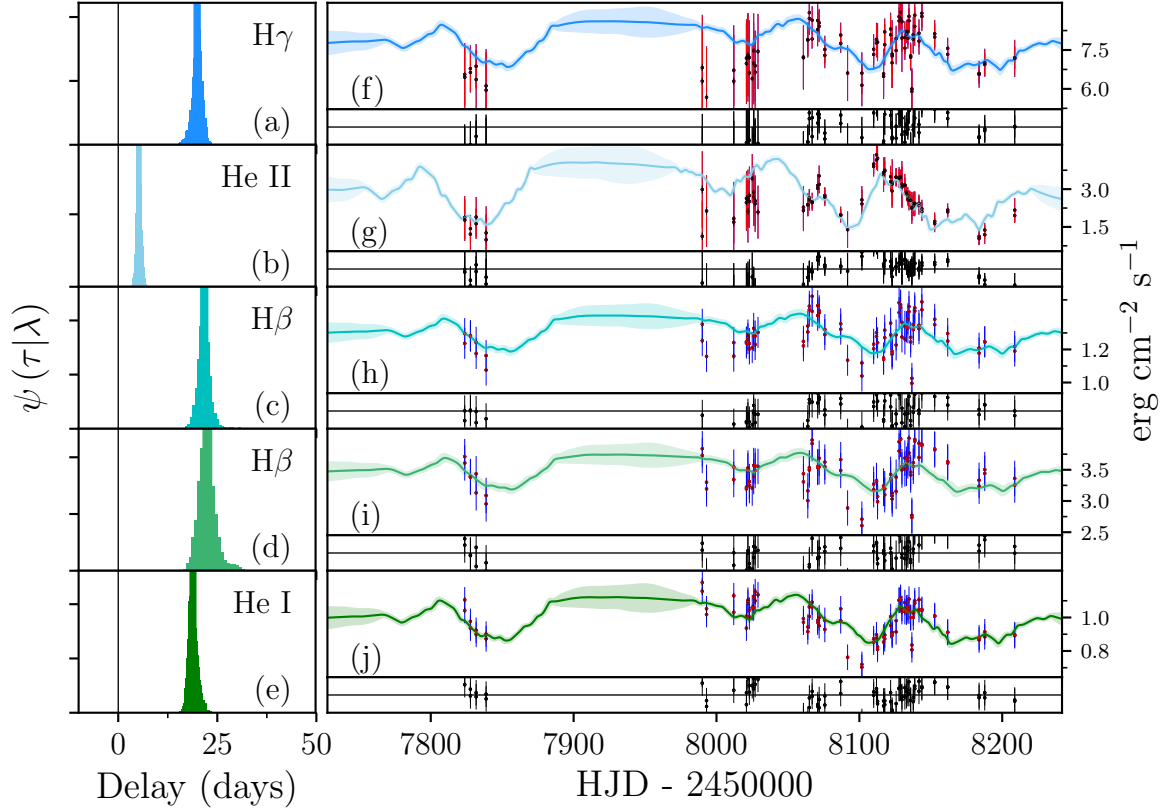
Figure 7. The inferred driving light curve, panel a in Figure 6 is also fit to the line light curves (panels f-j). Panels a-e show the posterior delay distributions, defined by CREAM's MCMC samples of the mean delay of top-hat response functions. The vertical line marks the zero delay. The light curves are Hγ λ4340, He II λ4686, Hβ λ4861 (blue-side), Hβ λ4861 (red-side) and He I λ5876 respectively. The units are 10^{-13} erg cm^{-2} s^{-1} for Hγ and He II, and 10^{-12} erg cm^{-2} s^{-1} for the other panels.
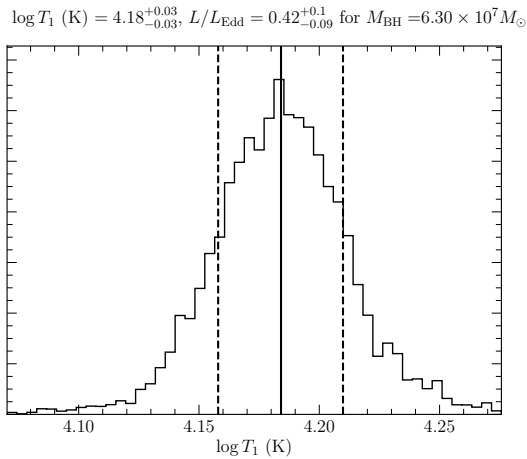
Figure 8. The posterior probability histogram for T_1 as derived by CREAM, for $\alpha = 3/4$ and $i = 0$.

Table 11. Host-galaxy subtracted fluxes for each wavelength (dust-corrected).

λ	Total	Galaxy	Total - Galaxy
(Å)	(mJy)	(mJy)	(mJy)
3656	7.604 ± 0.011	0	7.604 ± 0.011
4770	11.308 ± 0.009	3.553 ± 0.075	7.75 ± 0.08
5477	11.80 ± 0.01	4.32 ± 0.08	7.47 ± 0.08
6231	15.516 ± 0.013	7.974 ± 0.105	7.54 ± 0.11
7625	14.317 ± 0.015	7.089 ± 0.105	7.23 ± 0.11
8660	15.442 ± 0.016	8.806 ± 0.119	6.64 ± 0.12

5 BLACK HOLE MASS

There have been several previous campaigns (e.g. Peterson et al. 1998b, 2004; Pozo Nuñez et al. 2012; Kollatschny et al. 2014; Grier et al. 2017a; Du et al. 2018b) reporting BH mass estimates in 3C 120. To determine the BH mass, we require the emission-line time delay τ and velocity width ΔV. Combining these two parameters, we can estimate the mass of the BH using Eqn. (1), thus assuming that the gas motions in the BLR are dominated by the strong gravity of the cen-
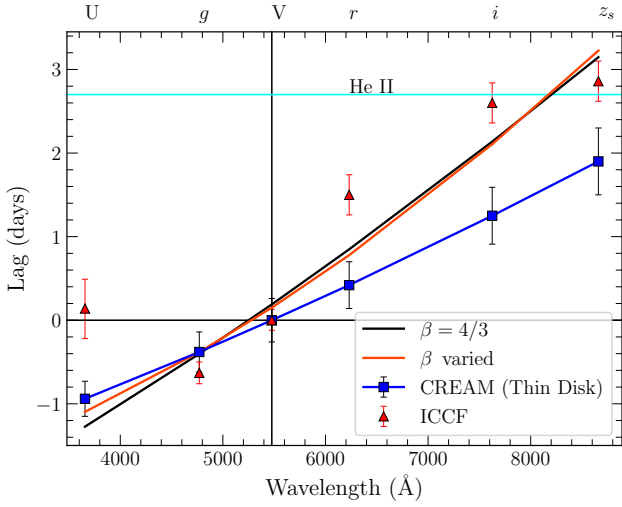
Figure 9. Lag as a function of wavelength relative to V band (shown by the vertical line). The best fits of τ_0 with $\beta = 4/3$ (black) and β allowed to vary (orange) are shown. The solid blue line is prediction from CREAM standard thin-disc theory with $L/L_{Edd} = 0.4$. The cyan solid line shows the broad He II emission-line lag of 2.7 days relative to V for comparison.
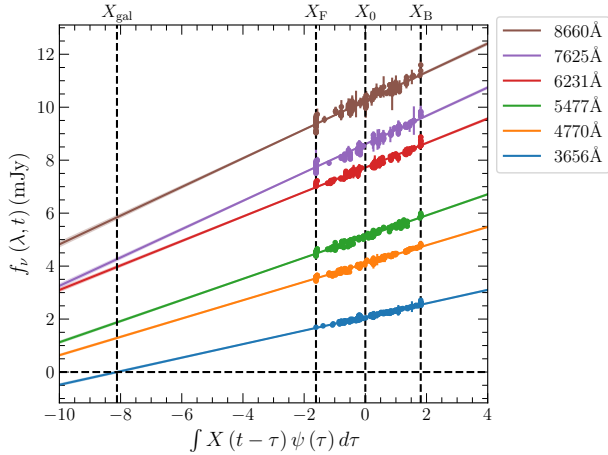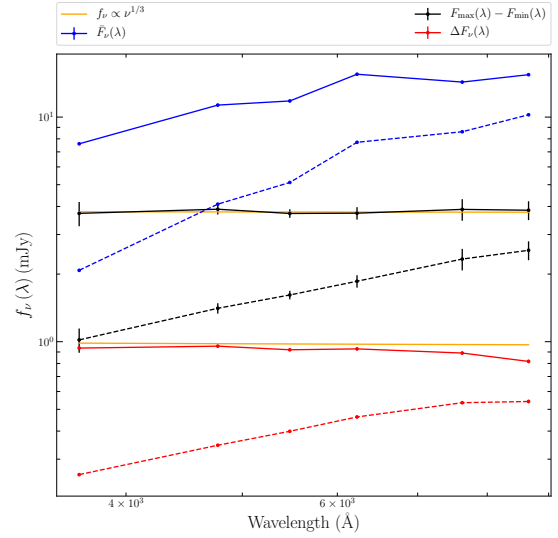

Figure 11. The log-log plot of the mean (disc+galaxy) spectrum (blue), rms disc spectrum (red) and max-min (black) disc spectrum, compared with the expected power-law slope (yellow). The dashed lines correspond to reddened spectra and solid lines to de-reddened spectra.
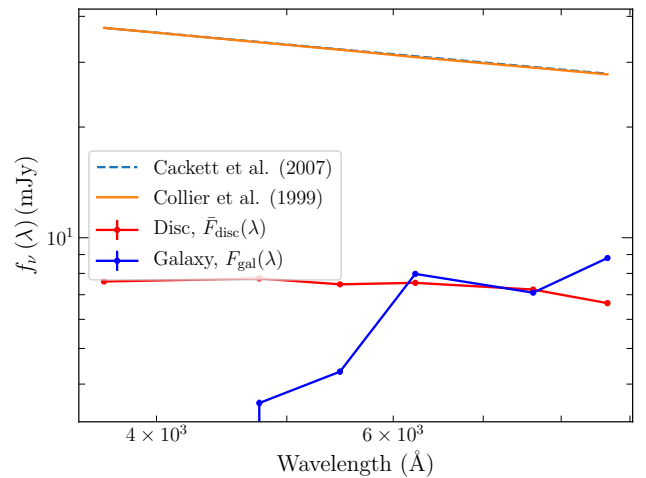

Figure 10. Model response light curves for the CREAM fits to the input light curves (not dust-corrected). The vertical lines label the driving light curve values used to evaluate the galaxy, faint-state, and bright state spectra (X_{gal}, X_F, X_B). At $X(t) = X_{gal} = -8.12$ the linear fit crosses zero at the shortest wavelength, placing a lower limit on the host-galaxy flux.

Figure 12. The predicted spectra are shown in blue (dotted) and orange (solid) estimated from the $T(r)$ profile derived from the CREAM fit to $\tau(\lambda)$, compared with the mean disc spectrum shown in red. The host-galaxy spectrum is in blue (solid).

tral BH.

We measure the velocity width and its uncertainty from the mean and rms spectra produced by PrepSpec (Section 2.3). Our linewidth measurements are listed in Table 4. Our measurements are generally consistent with those measured by Kollatschny et al. (2014) but with better statistical errors. We compare only with Kollatschny et al. (2014) because other papers report linewidths only for Hβ.

We use the velocity dispersion σ_{line} estimated from the rms spectrum in the calculation of the BH mass since

it yields less biased black hole mass measurements than FWHM (Peterson 2011). The dimensionless factor f in Eqn. 1 is different for each AGN. For comparison with similar studies on 3C 120, we adopt a mean factor of $\langle f \rangle = 5.5$ (Onken et al. 2004) estimated by bringing the $M_{BH} - \sigma_*$ relation into agreement with the same relation for quiescent galaxies. We also use our Hβ lag of $21.2^{+1.6}_{-1.0}$ days relative to the V-band continuum and linewidth ($\sigma_{line} = 1657 \pm 3$ km s^{-1}), to calculate the black hole mass. We measured our resulting mass of 3C 120 to be $M = \left(6.3^{+0.5}_{-0.3}\right) \times 10^7 \, (f/5.5) \, M_\odot$.

We compare our black hole mass estimate based on Hβ with the individual campaigns where the Hβ line was used to measure black hole mass in 3C 120 (Table 12 and Figure 13). Peterson et al. (2004) did a reanalysis of 3C 120 data and reported the Hβ lag of $39.4^{+22.1}_{-15.8}$ days with large uncertainty, accounting for the large errors on their derived black hole mass $M = \left(5.55^{+3.14}_{-2.25}\right) \times 10^7 \, (f/5.5) \, \mathrm{M}_\odot$. Grier et al. (2012) deduced a lag of $27.2^{+1.1}_{-1.1}$ days from JAVELIN, which performs better statistically especially on well-sampled data as in their campaign. Hence, the smaller uncertainties and led to a BH mass $M = \left(6.7^{+0.6}_{-0.6}\right) \times 10^7 \, (f/5.5) \, \mathrm{M}_\odot$. Recently, Du et al. (2018b) detected a lag of $20.2^{+5.0}_{-4.2}$ days which is similar to our Hβ lag in this work, and measured the black hole mass $M = \left(3.26^{+0.83}_{-0.71}\right) \times 10^7 \, (f/4.47) \, \mathrm{M}_\odot$. We combine the mass estimates and uncertainties from all measurements to produce the weighted mean (Barlow 2003) of the black hole mass $M = \left(6.2^{+0.3}_{-0.3}\right) \times 10^7 \, (f/5.5) \, \mathrm{M}_\odot$. We note that these BH mass measurements incorporate only the measurement uncertainties in τ and σ_{line}, they do not take into account the uncertainty in f. We intentionally did not include Peterson et al. (1998b) as no uncertainties were determined on their black hole mass. Generally, we find consistent mass estimates to within 1σ error limits except for Du et al. (2018b), possibly due to the significant difference in the Hβ linewidth and lag they measure compared to other studies since the black hole mass is a combination of these two parameters. We also plot the measured Hβ lags and rms linewidth in Figure 13 and see that they are generally consistent with the virial assumption (i.e the lags should decrease as the linewidth increases).

Grier et al. (2017a) measured the BH mass for 3C 120 to be $M = 6.92^{+1.38}_{-1.55} \times 10^7 \, M_\odot$, through dynamical modeling (Pancoast et al. 2014a,b) of the object's BLR. This way of measuring the mass does not assume a particular value of f and relies on direct modeling to measure the BH mass. It also eliminates the uncertainty introduced by assuming a value of f. Using mass derived from dynamical modeling, the virial factor f can be inferred for individual objects. Grier et al. (2017a) estimate f specific to 3C 120 of $f_\sigma = 5.75 \pm 2.25$ and $f_{\mathrm{FWHM}} = 6.46 \pm 2.53$, where σ is from the rms spectrum and FWHM is measured from the Grier et al. (2012) mean spectrum. The f adopted here is consistent with f inferred from dynamical modeling, leading to consistent black hole masses to within 1σ.

6   VELOCITY-RESOLVED LAG MEASUREMENTS

The ultimate goal of RM studies is to ascertain the geometry and kinematics of the BLR through mapping the responsivity of the line-emitting gas as a function of time lag and line-of-sight velocity. Well-conducted velocity-resolved studies can provide information about the distribution and velocity field of the emitting gas within the BLR, whether infall/inflow, outflow and/or Keplerian orbits. In an infall/inflow, longer lags are blueshifted having negative velocities and shorter lags are redshifted having positive velocities. In an outflow, the opposite pattern to that of an infall can be seen. Keplerian/circular orbits are symmetric
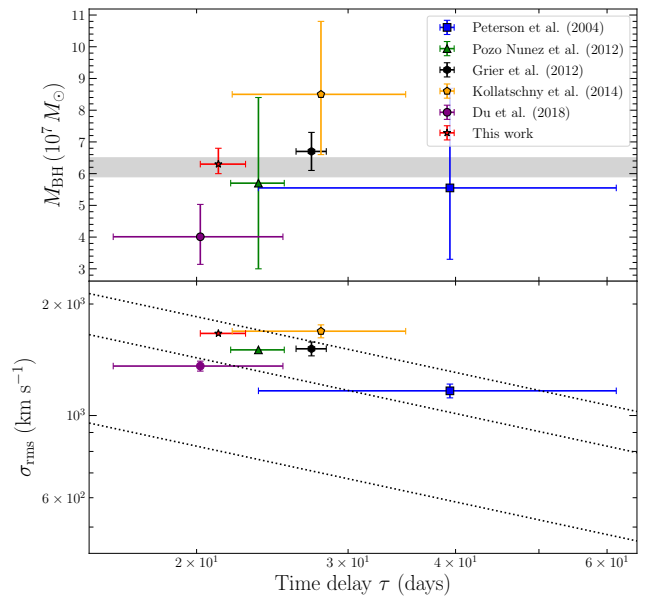

Figure 13. Top: The BH mass as a function of the Hβ time delay, shown are the different campaigns on 3C 120. The gray band indicates the 1σ envelope of the weighted average of the BH mass based on Hβ measurements. Bottom: The Hβ broad emission-line width as a function of the lag. From bottom to top, the dotted lines correspond to constant black hole masses of $2\times10^7 \mathrm{M}_\odot$, $6\times10^7 \mathrm{M}_\odot$, $1\times10^8 \mathrm{M}_\odot$ respectively for $f = 5.5$.

about zero velocity, with shorter lags on the wings of the profile (e.g. Welsh & Horne 1991; Bentz et al. 2009b; Denney et al. 2009b, 2010; Barth et al. 2011; Grier et al. 2013; Du et al. 2016; De Rosa et al. 2018).

We undertook velocity-resolved lag measurements across the Hβ emission-line profile in 3C 120. Previous studies (Grier et al. 2013, 2017a; Du et al. 2018b) have been successful in recovering the structure and kinematics of the BLR in 3C 120 using velocity-resolved lag measurements. We divided the Hβ emission-line profile into 11 velocity bins across the line in the continuum-subtracted spectra from -4000 km s^{-1} to 4000 km s^{-1}, using the FTN blue-side data. We set the zero-velocity using the wavelength of the Hβ line in rest frame to separate the blueshifted and redshifted measurements. We constructed Hβ light curves by integrating the line fluxes in each velocity bin.

We then measured the time lag (τ_{cen}) for each of the light curves with respect to the V-band continuum light curve using the ICCF, as in Section 3.2. We present our velocity-resolved results in the rest frame in Figure 14 based on the mean spectrum. Our Hβ velocity-resolved lag profile exhibits a pattern consistent with Keplerian/circular with longer lags at about zero velocity and shorter lags on the wings of the profile. The lag is $\tau \sim 25$ days near line centre and drops symmetrically to ~ 17 days at ± 4000 km s^{-1}. This is consistent with Grier et al. (2013) where they deduced a similar morphology.

Table 12. Outcomes of previous reverberation mapping studies on 3C 120.

Study	Campaign	Hβ lag (days)	σ_{line} (km s^{-1})	$M_{\text{BH}}^{\text{(b)}}$ ($10^7\,\text{M}_\odot$)	$\log \lambda L_\lambda$(5100Å) (erg s^{-1})
(1)	1989 − 1996	$39.4^{+22.1}_{-15.8}$	1166 ± 50	$5.55^{+3.14}_{-2.25}$	44.01 ± 0.05
(2)	2008 − 2009	$27.9^{+7.1}_{-5.9}$	1689 ± 68	$8.5^{+2.3}_{-1.9}$	44.12 ± 0.07
(3)	2009 − 2010	$23.6^{+1.7}_{-1.7}$	$1504^{\text{(c)}}$	$5.7^{+2.7}_{-2.7}$	43.84 ± 0.04
(4)	2010 − 2011	$27.2^{+1.1}_{-1.1}$	1514 ± 65	$6.7^{+0.6}_{-0.6}$	43.96 ± 0.06
(5)	2016 − 2017	$20.2^{+5.0}_{-4.2}$	1360 ± 42	$4.01^{+1.02}_{-0.87}$	$43.99 \pm 0.01^{*}$
(6)	2016 − 2018	$21.2^{+1.6}_{-1.0}$	1657 ± 3	$6.3^{+0.5}_{-0.3}$	43.99 ± 0.01
Mean[a]				$\mathbf{6.2^{+0.3}_{-0.3}}$	

(1) Peterson et al. (2004), (2) Kollatschny et al. (2014), (3) Pozo Nuñez et al. (2012), (4) Grier et al. (2012), (5) Du et al. (2018b), (6) This work.
[a] Weighted average.
[b] M masses calculated using $\langle f \rangle = 5.5$ for comparison.
[c] Measured from single-epoch spectra.
[*] The authors do not provide the measurement, we put that here because the two campaigns overlap.
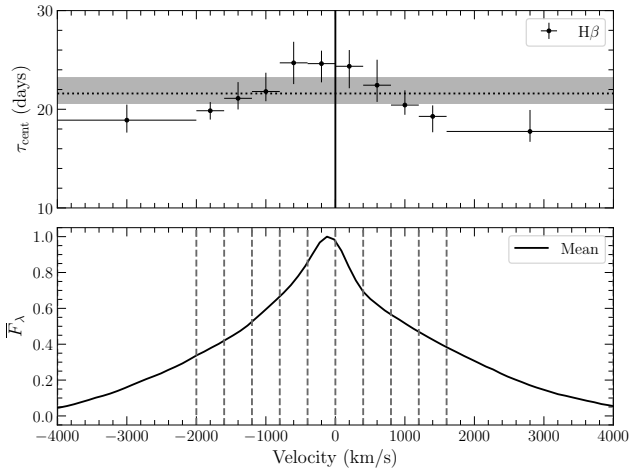

Figure 14. Velocity-resolved lags for the broad Hβ emission-line in 3C 120. The upper panel shows the measured centroid lags at different velocity bins. The dotted horizontal line is the average lag and the grey band its uncertainty (from Table 5). The lower panel shows the continuum-subtracted normalised mean spectrum. The dotted lines show the bins. Error bars in the horizontal direction represent the velocity bin size.

7 DISCUSSION

7.1 Mass Determination

Because of its nature, 3C 120 has been the subject of 5 previous spectroscopic reverberation mapping studies, thus providing a good sample of independent measurements in the literature to which we compare our results. Based on the ICCF and CREAM methods, we measure the lags of Hγ, He II λ4686, Hβ, and He I λ5876 in 3C 120 (Table 5). We find that both methods give consistent lag measurements

and small uncertainties. We therefore adopt lags from ICCF as our primary method.

We list the variability amplitudes for each of the broad emission lines in Table 5. He II λ4686 has a higher variability (30%) and shorter time delay (2 days) than do the Balmer and He I lines, suggesting it originates really close, within a few light days, of the ionising source. This may also be an indication of the BLR stratification in 3C 120 (Kollatschny 2003). We compare our measurements with Kollatschny et al. (2014), in which multiple-line lag measurements were also reported. We note that He II λ4686 lag is similar to V-band lag, suggesting the He II λ4686 emitting region is close to V emitting region (similar physical size). So we add back the V-band continuum lag to He II λ4686 for comparison with other lines, thus we end up with $5.0^{+0.8}_{-0.8}$ days.

Our Hβ measurement, combined with the previous studies indicate that the Hβ line time lag is decreasing since the first campaign (Table 12). Peterson et al. (2004) measured a long delay, 40 ± 20 days. Campaigns succeeding that measured shorter delays with much improved error estimates as a result of robust time delay measurement techniques such as JAVELIN in Grier et al. (2012) and better sampling. This decreasing trend in Hβ lag might be expected to correspond to a corresponding decrease in optical luminosity. The Hβ reverberations depend on the continuum level during the time of the monitoring campaign, such that longer time lags would correspond to higher continuum states (Cackett & Horne 2006). This expected correlation is not observed (Table 12).

Using the measured centroid lags of the Helium and Balmer lines, and their rms linewidths, we estimate black hole mass from each line, as listed in Table 13. We generally find that the black hole masses based on the individual lines are consistent to within 1σ uncertainties except for He II λ4686. The black hole mass is the combination of the lag

Table 13. Black hole masses for the individual lines.

Line	τ	$\sigma_{\rm rms}$	M
	(days)	(km s^{-1})	($M_\odot$)
(1)	(2)	(3)	(4)
Hγ	$18.8^{+1.3}_{-1.0}$	1786 ± 3	$6.4^{+0.3}_{-0.5}$
He II $\lambda4686$	$5.0^{+0.8}_{-0.8}$	2282 ± 2	$2.8^{+0.5}_{-0.5}$
Hβ	$21.2^{+1.6}_{-1.0}$	1657 ± 3	$6.3^{+0.5}_{-0.3}$
He I $\lambda5876$	$16.9^{+0.9}_{-1.1}$	2037 ± 12	$7.5^{+0.4}_{-0.5}$
			$\times10^7$

$\langle f \rangle = 5.5$

and velocity width. The rms spectrum in Figure 3 shows that the red wing of He II $\lambda4686$ is blended with the Hβ line, and this blending may lead to underestimation of the linewidth, and hence would affect the final black hole mass measurement.

7.2 BLR Geometry and Kinematics

Our high signal-to-noise and high cadence allowed us to carry out the velocity-resolved time lag analysis to probe the geometry and kinematics of the BLR in 3C 120 across the Hβ emission-line profile. Our velocity-resolved profile is shown in Figure 14. We see clearly a symmetric pattern about zero velocity consistent with Keplerian motions from −4000 km s^{-1} to +4000 km s^{-1}, with higher lags at about zero velocity and shorter lags on the wings. The line wings have almost identical delays with respect to the V-band continuum. This is interesting as it indicates that the velocity field is not dominated by radial inflow or outflow. There is an overall gravitational domination of the BLR gas motions by the black hole, thus validating the assumption (i.e gravity dominated system) that allow us to measure the mass of the central black hole.

Grier et al. (2013) also deduced a kinematics consistent with our findings but with an additional component, in which they interpreted their velocity-resolved lag measurement as a combination of circular orbits plus inflowing gas from the campaign 2010 – 2011. In an earlier campaign (2008 – 2009), Kollatschny et al. (2014) deduced a two-component BLR structure similar to that of Grier et al. (2013, 2017a). This is not surprising given the small time gap between these campaigns. The most recent campaign (2016 – 2017) is by Du et al. (2018b) in which they deduced from their Hβ velocity-resolved profile, a pattern consistent with an outflow from 1500 km s^{-1} to −1500 km s^{-1} in their rms spectrum, although with large error bars.

7.3 CREAM thin disc model

In addition to the broad emission-line variability studies, we also undertook the inter-band continuum variability studies in 3C 120 following our high signal-to-noise, densely sampled and highly correlated continuum light curves in six

bands spanning the wavelength range from 3656-8660Å. To investigate further this waveband correlation in terms of the standard thin-disc model, we fit the continuum light curves using CREAM's thin steady-state blackbody disc model ($T = T_1(r_1/r)^{3/4}$ with $T_1^4 \propto M\dot{M}/r_1^3$), in order to measure the disc temperature T_1 at $r = 1$ light day, and hence $\dot{M}$ for $M = 6.3 \times 10^7\, M_\odot$. Generally, the CREAM model fits the data quite well even with the sporadic variability in the broad lines. We find values of $T_1 = (1.51 \pm 0.10) \times 10^4$ K, mass accretion rate $\dot{M} = 0.60 \pm 0.15\, M_\odot {\rm yr}^{-1}$ and corresponding Eddington ratio $\dot{m}_{\rm Edd} = \dot{M}/\dot{M}_{\rm Edd} = L_{\rm bol}/L_{\rm Edd} = 0.42^{+0.10}_{-0.09}$, implying 3C 120 is accreting at about half the Eddington rate. Section 7.3.1 summarizes the results of the CREAM mean delays when compared with model-independent ICCF delays in terms of the $\tau - \lambda$ relation. Section 7.3.2 goes over the accretion disc spectrum and implications thereof.

7.3.1 Lag spectrum

The ICCF lag spectrum shows lag-wavelength dependence relation consistent with reprocessing model $\tau \propto \lambda^\beta$, when allowing the normalization factor τ_0 to vary and fixing β to 4/3. The excess U lag (i.e. greater than expected from extrapolating the longer-wavelength lags) is observed in Figure 9. The larger U lag than would be expected has been reported in previous inter-band continuum lag studies. For example, Edelson et al. (2015) and Fausnaugh et al. (2016) also detect this excess U lag, and link it to contamination by the broad emission lines and diffuse continuum (DC) from the BLR (e.g., Korista & Goad 2001). This DC contamination is signified by the Balmer jump at 3640Å and Paschen jump at 8200Å in Figure 9. This contamination tends to lead to disc sizes several times larger than expected from standard accretion thin-disc model (e.g., Fausnaugh et al. 2016; McHardy et al. 2018). In our analysis, we find the excess U-band lag (Figure 9), but with no corresponding excess U-band (Figure 11). If we compare ICCF's best-fit disc normalization τ_0 at λ_0 with CREAM, results in τ_0 that is a factor of 1.6 times larger, consistent with previous studies in which larger than expected values have been measured.

7.3.2 Accretion disc spectrum

Using CREAM's flux-flux method (Starkey et al. 2017), we investigate the origin of the UV/Optical continuum variability. In Figure 10, we observe linear relations with no significant curvature that would indicate a change in shape by the variable component across all the continuum light curves. This strong linear relationship implies that the variable component has a constant flux distribution (Winkler 1997), consistent with a disc reprocessing model. The slopes ΔF_ν of the best-fitting line of $f_\nu(\lambda, t)$ versus $X(t)$ give the spectrum of the variable component. We see that the spectral energy distribution (SED) of the variable spectrum resembles the $f_\nu \propto \lambda^{-1/3}$ spectrum expected for a steady-state blackbody accretion disc, after correcting for MW dust extinction. The intercepts $\bar{F}_\nu$ of the best-fitting line are used to derive the host-galaxy spectrum. We see that the variable component spectrum, after correcting for MW dust extinction, is very close to the $f_\nu \propto \nu^{1/3}$ spectrum predicted by standard thin-disc reprocessing model.
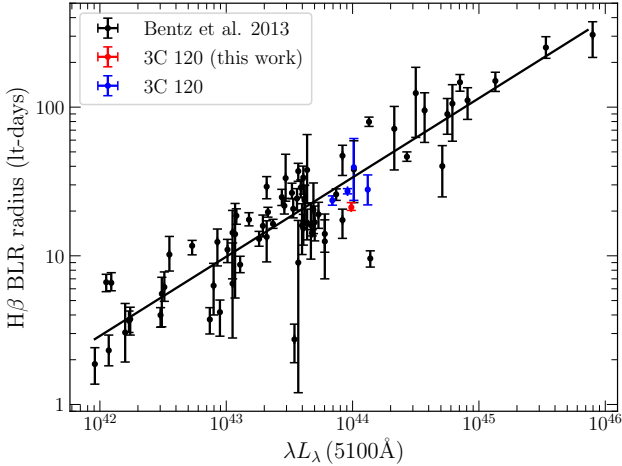
Figure 15. Optical continuum luminosity and Hβ lags for 3C 120 (this work) and other AGNs from Bentz et al. (2013).

Figure 16. $M_{BH} - \sigma_*$ relation of inactive galaxy sample (gray), compared with active galaxies with reverberation masses (blue). The reverberation masses were measured using a virial factor of $f = 5.2$. The solid lines are the best-fit lines to the reverberation sample ($\alpha = 8.00$ and $\beta = 3.55$) and inactive galaxy sample ($\alpha = 8.32$ and $\beta = 5.64$).

0.72 ± 0.10 with the intrinsic scatter of $\sigma_{int} = 0.43 \pm 0.08$ dex. McConnell & Ma (2013) measured $\alpha = 8.32 \pm 0.05$ and $\beta = 5.64 \pm 0.32$ for a sample of 72 quiescent galaxies. In both cases, we find that our target shows no significant deviation from the $M_{BH} - \sigma_*$ relation for quiescent galaxies and reverberation based samples.

7.4 Size-Luminosity Relation

Figure 15 examines the location of our Hβ lag measurement in the context of the $R_{BLR} - L$ relationship. We use CREAM's flux-flux analysis to determine the optical luminosity at 5100Å corresponding to our campaign, in a similar manner as, e.g., Winkler (1997); Pozo Nuñez et al. (2012). This led to $\lambda L_\lambda(5100) = 10^{43.99\pm0.01}$ erg s^{-1} after subtracting host-galaxy contribution estimated from Table 11. Figure 15 shows measurements of the size of the Hβ-emitting region as a function of the optical luminosity at 5100Å using measurements from Bentz et al. (2013). Our measurement is consistent with the general Hβ trend.

7.5 $M_{BH} - \sigma_*$ Relation

We also investigate if 3C 120 obeys the general trend of the scaling relations between M_{BH} and host-galaxy properties. We adopt the stellar velocity dispersion of 3C 120 of $\sigma_* = 162 \pm 20$ km s^{-1} reported in Nelson & Whittle (1995). We provide $M_{BH} - \sigma_*$ relation combining the samples of McConnell & Ma (2013) for inactive galaxies, and the reverberation-mapped AGN sample of Woo et al. (2010), along with our measurement of 3C 120 in Figure 16. The best-fit lines are characterized by

$$\log(M_{BH}/M_\odot) = \alpha + \beta \log(\sigma_*/200 \text{ km s}^{-1}) \quad (17)$$

For a sample of reverberation masses, Woo et al. (2010) measured $\alpha = 8.00 \pm 0.24$ and $\beta = 3.55 \pm 0.60$ assuming $\log f =$
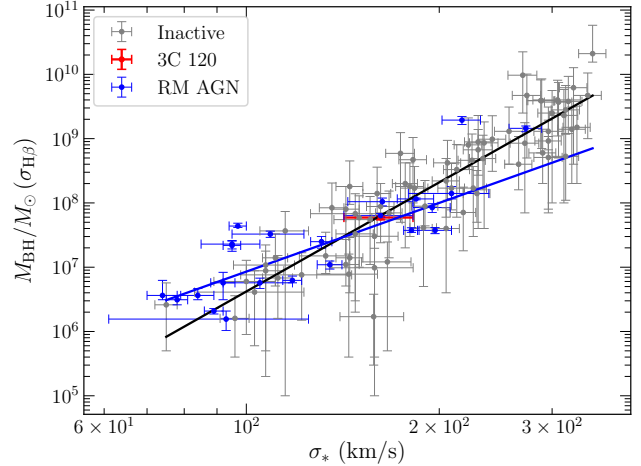
8 CONCLUSION

We carried out fully robotic photometric and spectroscopic observations of the well-studied broad-line radio galaxy 3C 120 with the Las Cumbres Observatory (LCO) from 2016 December to 2018 April as part of the LCO AGN Key Project on Reverberation Mapping of Accretion Flows. We summarize the main results as follows:

• We used the ICCF method alongside CREAM to carry out multiple-line (Hγ, He II λ4686, Hβ, He I λ5876) lag measurements in 3C 120. We find that the two techniques give consistent results to within uncertainties.

• We find lags relative to V of 2.7 days for He II and 15-18 days for He I and Balmer lines, consistent with a decrease in ionisation with radius.

• Combining the Hβ lag ($21.2^{+1.6}_{-1.0}$ days) relative to V, and its velocity dispersion ($\sigma_{line} = 1657 \pm 3$ km s^{-1}) in the rms spectrum, we infer a central black hole mass ($6.3^{+0.5}_{-0.3} \times 10^7 M_\odot$) that is in accord with results from previous studies after correcting to a common virial correction factor $f = 5.5$.

• From our velocity-resolved Hβ lag measurements, we deduced a symmetric pattern with a 25 day lag at line centre reducing to $\sim$ 17 days on both the blue and red wings of the line.

• Our inter-band continuum variability study reveals wavelength-dependent delays with longer delays at longer

wavelengths. The delays span 3 to 4 days, and are compatible with $\tau \propto \lambda^{4/3}$ apart from an excess of 1 or 2 days in the U-band.

• Our CREAM analysis, fitting a face-on reverberating steady-state black body disc model, finds $M\,M_\odot = 10^{7.58\pm0.11}\,M_\odot^2$/yr corresponding to $L/L_{\rm Edd} \sim 0.4$ for $M = 6.3 \times 10^7\,M_\odot$.

• We measure the size of the disc to be 1.6 times larger than the prediction from CREAM thin-disc theory with $L/L_{\rm Edd} \sim 0.4$, consistent with other RM continuum studies.

• The SED of the disc spectrum, isolated by variations, matches $F_\nu \propto \nu^{1/3}$ from disc theory with no sign of bound-free edges.

The CREAM thin-disc model generally fits the 3C 120 data relatively well. In the future, we want to explore departures from the thin-disc model by varying the inclination (from face-on), the power index α to see how it affects the mass accretion rate in 3C 120, and potentially the Eddington ratio in terms of the thin-disc theory. Due to the high quality of these observations, they lend themselves to potential further study for a more detailed model for 3C 120.

ACKNOWLEDGEMENTS

DATA AVAILABILITY

The data underlying this article are available in the article and in its online supplementary material.

REFERENCES

Antonucci R., 1993, ARA&A, 31, 473
Barlow R., 2003, in Lyons L., Mount R., Reitmeyer R., eds, Statistical Problems in Particle Physics, Astrophysics, and Cosmology. p. 250 (arXiv:physics/0401042)
Barth A. J., et al., 2011, ApJ, 743, L4
Barth A. J., et al., 2015, ApJS, 217, 26
Bentz M. C., Katz S., 2015, PASP, 127, 67
Bentz M. C., Peterson B. M., Pogge R. W., Vestergaard M., Onken C. A., 2006, ApJ, 644, 133
Bentz M. C., Peterson B. M., Netzer H., Pogge R. W., Vestergaard M., 2009a, ApJ, 697, 160
Bentz M. C., et al., 2009b, ApJ, 705, 199
Bentz M. C., et al., 2013, ApJ, 767, 149
Blandford R. D., McKee C. F., 1982, ApJ, 255, 419
Blanton M. R., Roweis S., 2007, AJ, 133, 734
Brown T. M., et al., 2013, PASP, 125, 1031
Cackett E. M., Horne K., 2006, MNRAS, 365, 1180
Cackett E. M., Horne K., Winkler H., 2007, MNRAS, 380, 669
Chambers K. C., et al., 2016, arXiv e-prints, p. arXiv:1612.05560
Chelouche D., Pozo Nuñez F., Kaspi S., 2019, Nature Astronomy, 3, 251
Collier S., Horne K., Wanders I., Peterson B. M., 1999, MNRAS, 302, L24
Collins K. A., Kielkopf J. F., Stassun K. G., Hessman F. V., 2017, AJ, 153, 77
De Rosa G., et al., 2018, ApJ, 866, 133
Denney K. D., Peterson B. M., Dietrich M., Vestergaard M., Bentz M. C., 2009a, ApJ, 692, 246
Denney K. D., et al., 2009b, ApJ, 704, L80
Denney K. D., et al., 2010, ApJ, 721, 715
Du P., et al., 2016, ApJ, 820, 27
Du P., et al., 2018a, ApJ, 856, 6
Du P., et al., 2018b, ApJ, 869, 142
Ducati J. R., Bevilacqua C. M., Rembold S. r. B., Ribeiro D., 2001, ApJ, 558, 309
Edelson R. A., Krolik J. H., 1988, ApJ, 333, 646
Edelson R., Turner T. J., Pounds K., Vaughan S., Markowitz A., Marshall H., Dobbie P., Warwick R., 2002, ApJ, 568, 610
Edelson R., et al., 2015, ApJ, 806, 129
Fausnaugh M. M., et al., 2016, ApJ, 821, 56
Fausnaugh M. M., et al., 2017, ApJ, 840, 97
Fausnaugh M. M., et al., 2018, ApJ, 854, 107
Ferrarese L., Ford H., 2005, Space Sci. Rev., 116, 523
Ferrarese L., Merritt D., 2000, ApJ, 539, L9
Fitzgerald M. P., 1970, A&A, 4, 234
Fitzpatrick E. L., 1999, PASP, 111, 63
Gaskell C. M., Peterson B. M., 1987, ApJS, 65, 1
Gaskell C. M., Sparke L. S., 1986, ApJ, 305, 175
Gebhardt K., et al., 2000, ApJ, 539, L13
Gómez J. L., Roca-Sogorb M., Agudo I., Marscher A. P., Jorstad S. G., 2011, ApJ, 733, 11
Grier C. J., et al., 2012, ApJ, 755, 60
Grier C. J., et al., 2013, ApJ, 764, 47
Grier C. J., Pancoast A., Barth A. J., Fausnaugh M. M., Brewer B. J., Treu T., Peterson B. M., 2017a, ApJ, 849, 146
Grier C. J., et al., 2017b, ApJ, 851, 21
Grier C. J., et al., 2018, ApJ, 868, 76
Henden A. A., Levine S., Terrell D., Welch D. L., 2015, in American Astronomical Society Meeting Abstracts #225. p. 336.16
Jiang Y.-F., et al., 2017, ApJ, 836, 186
Kaspi S., Smith P. S., Netzer H., Maoz D., Jannuzi B. T., Giveon U., 2000, ApJ, 533, 631
Kollatschny W., 2003, A&A, 407, 461
Kollatschny W., Ulbrich K., Zetzl M., Kaspi S., Haas M., 2014, A&A, 566, A106
Korista K. T., Goad M. R., 2001, ApJ, 553, 695
Korista K. T., Goad M. R., 2019, MNRAS, 489, 5284
Kormendy J., Gebhardt K., 2001, in Wheeler J. C., Martel H., eds, American Institute of Physics Conference Series Vol. 586, 20th Texas Symposium on relativistic astrophysics. pp 363–381 (arXiv:astro-ph/0105230), doi:10.1063/1.1419581
Kormendy J., Richstone D., 1995, ARA&A, 33, 581
Lawther D., Goad M. R., Korista K. T., Ulrich O., Vestergaard M., 2018, MNRAS, 481, 533
Li J., et al., 2017, ApJ, 846, 79
Li Y.-R., Zhang Z.-X., Jin C., Du P., Cui L., Liu X., Wang J.-M., 2019, arXiv e-prints, p. arXiv:1909.04511
Lynden-Bell D., Rees M. J., 1971, MNRAS, 152, 461
Magorrian J., et al., 1998, AJ, 115, 2285
McConnell N. J., Ma C.-P., 2013, ApJ, 764, 184
McHardy I. M., et al., 2018, MNRAS, 480, 2881
Nelson C. H., Whittle M., 1995, ApJS, 99, 67
Onken C. A., Ferrarese L., Merritt D., Peterson B. M., Pogge R. W., Vestergaard M., Wandel A., 2004, ApJ, 615, 645
Pancoast A., Brewer B. J., Treu T., 2014a, MNRAS, 445, 3055

Pancoast A., Brewer B. J., Treu T., Park D., Barth A. J., Bentz M. C., Woo J.-H., 2014b, MNRAS, 445, 3073

Pauliny-Toth I. I. K., Kellermann K. I., 1966, ApJ, 146, 634

Peterson B. M., 1993, PASP, 105, 247

Peterson B. M., 2001, in Aretxaga I., Kunth D., Mújica R., eds, Advanced Lectures on the Starburst-AGN. p. 3 (arXiv:astro-ph/0109495), doi:10.1142/9789812811318_0002

Peterson B. M., 2011, arXiv e-prints,

Peterson B. M., Wanders I., Horne K., Collier S., Alexander T., Kaspi S., Maoz D., 1998a, PASP, 110, 660

Peterson B. M., Wanders I., Bertram R., Hunley J. F., Pogge R. W., Wagner R. M., 1998b, ApJ, 501, 82

Peterson B. M., et al., 2004, ApJ, 613, 682

Peterson B. M., et al., 2013, ApJ, 779, 109

Pozo Nuñez F., Ramolla M., Westhues C., Bruckmann C., Haas M., Chini R., Steenbrugge K., Murphy M., 2012, A&A, 545, A84

Ramolla M., et al., 2018, A&A, 620, A137

Rodríguez-Pascual P. M., et al., 1997, ApJS, 110, 9

Sakata Y., et al., 2010, ApJ, 711, 461

Sargent W. L. W., 1967, PASP, 79, 369

Schlegel D. J., Finkbeiner D. P., Davis M., 1998, ApJ, 500, 525

Shakura N. I., Sunyaev R. A., 1973, A&A, 24, 337

Shen Y., et al., 2015, ApJS, 216, 4

Shen Y., et al., 2016, ApJ, 818, 30

Starkey D. A., Horne K., Villforth C., 2016, MNRAS, 456, 1960

Starkey D., et al., 2017, ApJ, 835, 65

Sun M., Grier C. J., Peterson B. M., 2018, PyCCF: Python Cross Correlation Function for reverberation mapping studies, Astrophysics Source Code Library (ascl:1805.032)

Urry C. M., Padovani P., 1995, PASP, 107, 803

Valenti S., et al., 2015, ApJ, 813, L36

Vestergaard M., 2002, ApJ, 571, 733

Walker R. C., 1997, ApJ, 488, 675

Wandel A., Peterson B. M., Malkan M. A., 1999, Astronomische Nachrichten, 320, 319

Welsh W. F., 1999, PASP, 111, 1347

Welsh W. F., Horne K., 1991, ApJ, 379, 586

White R. J., Peterson B. M., 1994, PASP, 106, 879

Winkler H., 1997, MNRAS, 292, 273

Woo J.-H., et al., 2010, ApJ, 716, 269

Zhang Z.-X., et al., 2019, ApJ, 876, 49

Zu Y., Kochanek C. S., Peterson B. M., 2011, ApJ, 735, 80

van Dokkum P. G., 2001, PASP, 113, 1420

APPENDIX A: ADDITIONAL TABLES

This paper has been typeset from a TeX/LaTeX file prepared by the author.

Table A1. Continuum light curve data

HJD − 2450000 (days)	Flux (mJy)	Error (mJy)	Band
7970.851	2.471	0.099	U
7970.855	2.298	0.078	U
7971.278	2.229	0.080	U
7971.282	2.257	0.075	U
7974.237	2.469	0.214	U
7818.909	3.871	0.054	g'
7818.911	3.736	0.051	g'
7819.266	3.828	0.032	g'
7819.268	3.752	0.031	g'
7820.265	3.772	0.032	g'
7751.044	5.322	0.017	V
7751.048	5.285	0.014	V
7756.114	5.226	0.013	V
7756.118	5.206	0.013	V
7760.362	5.184	0.017	V
7818.924	7.177	0.078	r'
7818.925	7.190	0.064	r'
7821.276	7.288	0.046	r'
7821.278	7.120	0.045	r'
7822.269	7.272	0.046	r'
7818.927	7.923	0.067	i'
7818.929	7.846	0.067	i'
7821.280	7.946	0.046	i'
7821.282	7.890	0.047	i'
7822.273	7.961	0.045	i'
7818.932	9.356	0.069	z_s
7818.935	9.544	0.066	z_s
7819.971	9.448	0.120	z_s
7819.974	9.393	0.181	z_s
7821.284	9.518	0.049	z_s

[Note] The full table is available online.

Table A2. Emission-line light curve data

HJD − 2450000 (days)	Flux (10^{-12} erg s^{-1}cm^{-2})	Error (10^{-12} erg s^{-1}cm^{-2})	Light Curve
7823.763	1.524	0.026	Hγ
7823.785	1.503	0.030	Hγ
7827.749	1.579	0.021	Hγ
7827.770	1.538	0.022	Hγ
7831.756	1.596	0.022	Hγ
7823.763	0.360	0.031	He II λ4686
7823.785	0.330	0.034	He II λ4686
7827.749	0.203	0.025	He II λ4686
7827.770	0.269	0.026	He II λ4686
7831.756	0.313	0.026	He II λ4686
7823.763	3.140	0.029	Hβ blue-side
7823.785	2.994	0.032	Hβ blue-side
7827.749	3.101	0.026	Hβ blue-side
7827.770	3.085	0.027	Hβ blue-side
7831.756	2.999	0.027	Hβ blue-side
7823.763	4.533	0.025	Hβ red-side
7823.785	4.458	0.027	Hβ red-side
7827.749	4.231	0.022	Hβ red-side
7827.770	4.224	0.024	Hβ red-side
7831.756	4.253	0.024	Hβ red-side
7823.763	1.087	0.016	He I λ5876
7823.785	1.027	0.017	He I λ5876
7827.749	0.961	0.014	He I λ5876
7827.770	0.913	0.015	He I λ5876
7831.756	0.899	0.015	He I λ5876

$^{\text{Note}}$ The full table is available online.